THE ASTROPHYSICAL JOURNAL, 390:602–621, 1992 May 10

GAMMA-RAY DEPOSITION AND NONTHERMAL EXCITATION IN SUPERNOVAE

CECILIA KOZMA AND CLAES FRANSSON
Stockholm Observatory, S-133 36 Saltsjöbaden, Sweden
Received 1991 July 16; accepted 1991 October 25

ABSTRACT

We calculate the γ-ray deposition in supernovae by solving the Spencer-Fano equation. Ionization, excitation, and heating rates are presented for the different chemical composition zones of a core collapse supernova, as well as for a solar composition applicable to for example, active galactic nuclei. We also discuss the thermalization in pure helium, oxygen, and iron plasmas. The latter is of particular interest for Type Ia supernovae. Convenient analytical expressions are given to facilitate the use of these results for the calculation of the physical conditions and emission from supernovae. We also discuss the spectral characteristics of the emission following nonthermal excitation and ionization in the supernova. In particular, we calculate the fraction of the absorbed γ-ray energy which is reemitted as UV photons with energy above 3.4 eV, the $n = 2$ threshold of hydrogen. We apply these results to the ionization of hydrogen and the formation of the Hα line. Good qualitative and quantitative agreement between the model and observations of SN 1987A are found. In particular, we find that absorption of UV photons in the Balmer continuum dominates the excitation before $\sim$500 days, while direct nonthermal excitation from the ground state dominates thereafter. We also discuss how the wing of the Hα line can be used as a probe of the density in the envelope.

Subject headings: atomic processes — gamma rays: theory — stars: individual (SN 1987A) — supernovae: general

1. INTRODUCTION

Observations of SN 1987A, as well as of other supernovae, provide strong evidence that most Type II and Ib supernovae are powered by radioactive decay of ^{56}Ni. This has for a long time been the standard model for Type Ia supernovae (Colgate & McKee 1969). On a time scale of 8.8 days, ^{56}Ni first decays to ^{56}Co, and then to ^{56}Fe on a time scale of 111.26 days. After a month only the emission from ^{56}Co is of interest. The radioactive decays mainly result in γ-rays with energies of $\sim$1 MeV, which Compton scatter off free and bound electrons in the medium, resulting in high-energy electrons with energies of $\sim$0.01–1 MeV. These deposit their energy by heating the thermal, free electrons, or by ionizing and exciting atoms and ions, giving rise to a cascade of electrons with different energies. In addition, the ionizations produce a large number of secondary electrons, which adds a nonlinearity to the cascade. The number of electrons per unit energy represents the degradation spectrum. Once the degradation spectrum is known, the fractions going into heating, excitation, and ionization can be calculated. The only important free parameters are the electron fraction and the chemical composition.

Understanding the thermalization of the γ-rays is important primarily for the interpretation and qualitative modeling of the supernova spectrum (e.g., Axelrod 1980; Fransson & Chevalier 1987, 1989; Swartz 1989, 1991; Xu & McCray 1991a; Lucy 1991). Accurate calculations of the nonthermal deposition applicable to supernovae are, however, to a large extent lacking. In this paper we calculate the deposition from the Boltzmann equation, using the best current available atomic data.

The nonthermal electron deposition has been studied by several authors in various other contexts. Most of these have been concerned with completely neutral plasmas, where scattering off free electrons has been neglected. Examples in the auroral context are the calculations by Peterson & Green (1968) for He I, Stolarski & Green (1967) for O I, N$_2$, and O$_2$, and Dalgarno & Lejeune (1971) for O I. For environments with a large population of free electrons, calculations exist for plasmas consisting of H and He (Spitzer & Tomasko 1968; Shull 1979; Shull & Van Steenberg 1985; Xu & McCray 1991a, b), and of H$_2$ and He (Voit 1991). For metal-dominated plasmas Fransson & Chevalier (1989) did Monte Carlo calculations, where O I was fully treated with both ionizations and excitations, while for most of the other elements only ionizations were included. In this paper we discuss all elements of interest for supernovae, including excitations, as well as an updated set of cross sections for ionizations, and where available, autoionizations. The energy deposition is sensitive to the composition, and we discuss a number of cases representing the various nuclear burning shells in a core collapse supernova. We also give results for a plasma of solar composition. This case is also of interest for the emission-line region in active galactic nuclei. The results are given in parametric form suitable for other users.

As an application of these results we discuss the ionization and radiative emission from the different composition regions, using analytical models. In particular, we calculate the efficiency of the conversion of the nonthermal energy into excitation and recombination emission from the various ions. The most important case is the conversion into Hα, which is explained quantitatively by this model.

In § 2 we describe the formalism used in our calculations, and in § 3 the results for the nonthermal deposition are given, both for single element compositions and for specific compositions. In § 4 we estimate the emission from the different zones and discuss the formation of the Hα line. Finally, we summarize our conclusions in § 5.

2. METHOD OF CALCULATION

When high-energy electrons pass through a medium they deposit their energy into three channels, heating, excitation, and ionization of the ambient medium. Through Coulomb scattering by thermal electrons, the fast electrons lose some of their energy in heating the medium. This energy loss is given by

$$L_e(E) \equiv -\left(\frac{dE}{dx}\right)_e = n_e \frac{2\pi e^4}{E} \ln\left(\frac{2E}{\zeta_e}\right) \qquad (1)$$

for $E > 14$ eV, and

$$L_e(E) \equiv -\left(\frac{dE}{dx}\right)_e = n_e \frac{2\pi e^4}{E} \ln\left(\frac{m_e v^3}{\gamma e^2 \omega_p}\right) \qquad (2)$$

for $kT \ll E < 14$ eV, where

$$\zeta_e = \frac{h}{2\pi}\,\omega_p = \frac{h}{2\pi}\left(\frac{4\pi n_e e^2}{m_e}\right)^{1/2} , \qquad (3)$$

and γ is Euler's constant (Schunk & Hays 1971). The logarithm in equations (1) and (2) is the only place where the total density enters in the calculations. The results below are therefore insensitive to the actual value of the total density.

To determine the excitation and ionization losses, accurate cross sections have to be used for all transitions, from the threshold energy up to several keV. At high energies the cross sections, both for ionization and allowed bound-bound transitions, are well described by the Bethe approximation, $\sigma \propto \ln(E)/E$. This is the same energy dependence as for the heating of the thermal electrons. Forbidden transitions only differ by the absence of the logarithmic factor, $\sigma \propto 1/E$. The sources of the different excitation and ionization cross sections are given in the Appendix.

Ionizations by the primary electrons create additional electrons, which contribute to all three channels. The distribution of secondary electrons as a function of the primary electron energy, E_p, and the secondary electron energy, E_s, is experimentally found to be well described by

$$P(E_p, E_s) = \frac{1}{J \arctan\,[(E_p - I)/2J]}\,\frac{1}{[1 + (E_s/J)^2]} \qquad (4)$$

(Opal, Petersen, & Beaty 1971). By convention, the outgoing electron with the lowest energy is called the secondary electron. I is the ionization potential, and J is a parameter specific for each element. J has the character of a cutoff energy for the secondary electrons. Opal et al. (1971), have measured J for a few elements and find for He I $J = 15.8$ eV, Ne I $J = 24.2$ eV, and Ar I $J = 10.0$ eV. For other elements we take $J = 0.6I$.

Let $\sigma_c(E, \epsilon)$ be the differential cross section for ionization, where E is the energy and ϵ the energy loss of the primary electron. The energy of the secondary electron, E_s, is therefore $E_s = \epsilon - I$. If $\sigma_c(E)$ is the total ionization cross section for an element, i, at an energy E, then

$$\sigma_c(E, \epsilon) = \sigma_c(E)P(E, \epsilon - I) . \qquad (5)$$

There are several methods of calculating the deposition of the high-energy electrons. The most straightforward is the Monte Carlo method, which follows each electron as it deposits its energy into the different channels (Shull & Van Steenberg 1985; Fransson & Chevalier 1989). The problem with this method is that if one wants to study rare channels, a large number of electrons have to be followed, which can be time consuming. Another approach, which we follow in this paper, is to solve the Boltzmann equation, which in this context was first formulated by Spencer & Fano (1954). In addition to atomic gases, this has been applied to the slowing down of particles in molecular gases (Inokuti 1990, and references therein).

The degradation spectrum is defined so that $y(E)dE$ is the flux of electrons in the energy interval $(E, E + dE)$. The Spencer-Fano equation is a special form of the Boltzmann equation, balancing the number of electrons leaving and entering the energy interval dE. For a medium containing only a single element with number density n, the balance can be written

$$\begin{aligned} y(E)n\left[\sum_j \sigma_j(E) + \int_I^{(I+E)/2} \sigma_c(E, \epsilon)d\epsilon\right] - \frac{d}{dE}\,[y(E)L_e(E)] \\ = n\left[\sum_j y(E + E_j)\sigma_j(E + E_j) + \int_I^{\lambda} y(E + \epsilon)\sigma_c(E + \epsilon, \epsilon)d\epsilon \right. \\ \left. + \int_{2E+I}^{E_{\max}} y(E')\sigma_c(E', E + I)dE'\right] + S(E) , \qquad (6) \end{aligned}$$

where $\lambda = \min\,(E_{\max} - E, E + I)$, $E_{\max}$ is the maximum energy of an electron, E_j is the excitation energy, and σ_j is the excitation cross section. (Spencer & Fano 1954; Douthat 1975a, b; Xu 1989; Xu & McCray 1991b). The left-hand side represents the number of electrons ejected from an energy interval dE, while the right-hand side gives the number of electrons injected into the same interval. The first and second terms on the left are the number of electrons leaving the energy interval dE through excitation and ionization, and the third term is the heating contribution. The ionization integral is taken from I, the ionization potential, to $(E + I)/2$, since the secondary electron is defined to be the electron with the lowest energy after the ionization. The first term on the right is the number of electrons entering the interval through excitation. The second and third terms are due to the primary and secondary electrons resulting from ionizations. The last term, $S(E)$, is the source term. For injection energies higher than $\sim$1 keV the results are independent of the input electron spectrum described by $S(E)$. This is a result of the similar high-energy behavior of the ionization, excitation, and Coulomb scattering cross sections (see above). For a mixture of several elements the Spencer-Fano equation is generalized to a trivial summation over the different elements and their levels. To solve the equation for $y(E)$, one only needs the values of y for energies larger than E. A straightforward method is an iterative scheme starting with $y(E_{\max})$, and then successively continuing to lower energies (see Xu 1989).

For numerical reasons it is more efficient to work with an integral version of the Spencer-Fano equation. Integrating equation (6) from E to $E_{\max}$ one gets

$$\begin{aligned} n\sum_j \int_E^{E+E_j} y(E')\sigma_j(E')dE' + n\int_E^{E_{\max}} y(E')\int_{E'-E}^{(E'+I)/2} \sigma_c(E', \epsilon)d\epsilon\, dE' \\ + y(E)L_e(E) = n\int_{2E+I}^{E_{\max}} y(E')\int_{E+I}^{(E'+I)/2} \sigma_c(E', \epsilon)d\epsilon\, dE' \\ + \int_E^{E_{\max}} S(E')dE' . \qquad (7) \end{aligned}$$

In this integral version there are only integrals of the form $\int \sigma_c(E, \epsilon)d\epsilon$, which can be calculated analytically, using equation (4), and only the total inelastic cross section enters. In the original equation (6), one must numerically integrate over the differential cross sections, and as these are steeply increasing at small energies, it is difficult to achieve high accuracy. In addition equation (6) is solved by iteration, which is time consuming. Equation (7), on the other hand, is an integral equation, which can be directly inverted, using standard matrix technique.

Once the degradation spectrum is known, the fractions going into heating, η_h, excitation of ion i to level j, η_{ij}, and ionization, η_{ic}, can be calculated from

$$\eta_h = \frac{1}{E_{\rm init}} \int_{E_0}^{E_{\rm max}} y(E')L_e(E')dE' + \frac{1}{E_{\rm init}} E_0\, y(E_0)L_e(E_0) + \frac{1}{E_{\rm init}} \int_0^{E_0} N(E')E'dE' , \quad (8)$$

$$\eta_{ij} = \frac{n_i E_{ij}}{E_{\rm init}} \int_{E_{ij}}^{E_{\rm max}} y(E')\sigma_{ij}(E')dE' , \quad (9)$$

$$\eta_{ic} = \frac{n_i I_i}{E_{\rm init}} \int_{I_i}^{E_{\rm max}} y(E')\sigma_{ic}(E')dE' , \quad (10)$$

where

$$N(E) = \sum_i n_i \Bigg[\sum_j y(E + E_{ij})\sigma_{ij}(E + E_{ij}) + \int_{I_i}^{\lambda_i} y(E + E')\sigma_{ic}(E + E', E')dE' + \int_{2E+I_i}^{E_{\rm max}} y(E')\sigma_{ic}(E', E + I_i)dE' \Bigg] + S(E) \quad \text{for } E \le E_0 . \quad (11)$$

$E_{\rm init}$ is the mean energy of the initial electrons, and E_0 the lowest excitation or ionization energy. These expressions agree with the expressions also derived by Xu & McCray (1991b). Xu & McCray also discuss how the fractional degradation losses can be calculated directly without explicitly calculating the spectrum, starting at low energy and gradually stepping up in energy, similarly to what is done in Monte Carlo simulations.

The sum of the fractions given in equations (8)–(10) is equal to one, as can be seen from multiplying equation (6) by E and integrating over energy from zero to $E_{\rm max}$. There are two alternative boundary conditions for the high-energy injection, of the nonthermal electrons. In this paper we use a constant, normalized source function over an interval ΔE such that $\int_{E_{\rm max}-\Delta E}^{E_{\rm max}} S(E)dE = 1$. In this case $y(E_{\rm max}) = 0$ and $E_{\rm init} = \int_0^{E_{\rm max}} ES(E)dE$. An alternative boundary condition is to inject all electrons at $E_{\rm init} = E_{\rm max}$, with $S(E) = 0$ and $y(E_{\rm max}) = 1/L_e(E_{\rm max})$. A drawback with the second boundary condition is that the degradation spectrum displays many sharp spikes at high energies due to the discrete nature of the excitation and ionization processes, and therefore becomes more time consuming and less accurate to integrate. For this reason we favor the first alternative. This is also closer to the actual case, since the electrons created by the Compton scattering have a broad range of energies.

Since only a fraction η_{ic} goes into ionization of an element i, one can define an effective ionization potential for the element by

$$\chi_{{\rm eff},\, i}(x_e) = \frac{I_i X_i}{\eta_{ic}(x_e)} , \quad (12)$$

where I_i is the ionization potential and X_i is the number fraction for the element. The ionization rate per unit volume is then

$$\Gamma_c n_i = \frac{4\pi J_\gamma \sigma_{\gamma,i}}{\chi_{{\rm eff},i}(x_e)} n_i , \quad (13)$$

where J_γ is the γ-ray mean intensity and $\sigma_{\gamma,i}$ the energy-averaged cross section for absorption by the ion i, which depends on the density and γ-ray source distributions. Under a fairly general range of conditions Fransson & Chevalier (1989) find that $\kappa_\gamma = 0.06(Z_i/A_i)$ cm^2 g^{-1}, implying that, $\sigma_{\gamma,i} = 0.06 Z_i m_p$ cm^2. Here Z_i is the nuclear charge of the ion and A_i the atomic weight.

3. RESULTS

3.1. *General Considerations*

To illustrate the general features of this problem, the degradation spectrum, $y(E)$, is plotted in Figure 1 as a function of energy for $x_e = 0.01$ for a pure oxygen plasma. The spectrum of the injected high-energy electrons is taken to be constant in the interval 2.9–3.0 keV in all calculations. For the density in equation (3) we use $n_e = 10^8$ cm^{-3}. This choice is unimportant for the results. Down to ~500 eV the spectrum in Figure 1 reflects the slowing down of the primary electrons. The sharp rise at low energies is a result of the distribution of the secondary electrons, which drops off above ~$3J$ ~ 30 eV (eq. [4]). Figure 2 shows the energy fractions going into heating, excitation, and ionization for oxygen as a function of energy. For energies below the lowest excitation and ionization potentials heating by the secondary electrons is the only permitted channel. Excitation dominates ionization at lower energies, while at higher energies the opposite is the case.

The main parameter determining the energy going into the different channels is, apart from the composition, the electron fraction, x_e. For large values of x_e most energy goes into heating of the thermal electrons, while for small x_e more energy goes into ionization and excitation. The reason is that the energy loss through Coulomb scattering is proportional to the electron density (eqs. [1] and [2]), while the fractions going

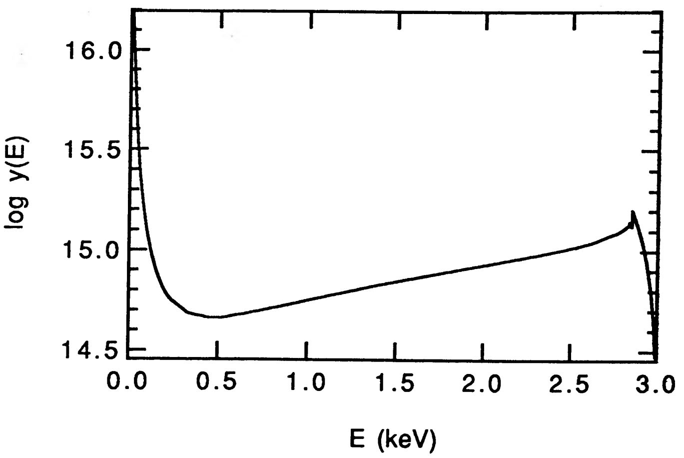

FIG. 1.—Electron degradation spectrum for a pure oxygen plasma at $x_e = 10^{-2}$. Above ~500 eV most of the spectrum reflects the energy loss of the primary electrons. The rise at low energies is due to secondary electrons, created by collisional ionizations.

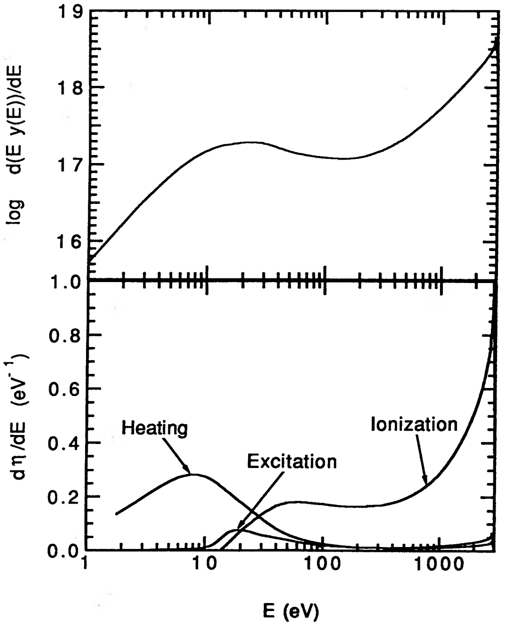

FIG. 2.—Fraction of the energy going into heating, excitation, and ionization as a function of energy for an oxygen plasma at $x_e = 10^{-2}$. The energy input to the various channels per logarithmic energy interval is proportional to $Ey(E)$, and we therefore plot this quantity in the upper panel for comparison. The thermal heating at low energies is mainly due to the secondary electrons. while the ionization and excitation contributions are dominated by the primary electrons at higher energies.

into excitation and ionization for an element are proportional to the number density of this element (eqs. [9] and [10]). As x_e increases, the fraction of neutral elements decreases, and the cross sections for excitation and ionization of the ionized species are smaller than for the neutral elements. But even at small x_e a finite amount goes into heating, because all the energy of the electrons with energies smaller than the lowest excitation energy goes into heating. This is formally seen from equation (8), where the last term gives the fraction of the energy going into heating, independent of x_e.

3.2. *Single Element Compositions*

In this section we give results for three single elements, helium, oxygen, and iron. These are of special interest, since they are dominant in the most important shells in core collapse supernovae. In contrast to § 3.3, we neglect the influence of other elements. Figures 3, 4, and 5 show the fractions going into heating, excitation, and ionization as a function of the electron fraction for the three cases. The number of levels included were for O I, 15, O II, 3, and He I, 10. For Fe I and Fe II the excitation cross sections are based on the Bethe approximation, with oscillator strengths taken from the compilation in Axelrod (1980). To handle the large number of transitions, ~139 for Fe I and ~224 for Fe II, we have summed over the different levels of the multiplets, according to their statistical weights and oscillator strengths.

The excitation-to-ionization ratio for an element reflects the relative cross sections for these processes. Helium has the highest ionization and excitation potentials of the three elements, and thus a larger portion goes into heating for this element. The ratio of the integrated excitation cross section to the ionization cross section is largest for Fe I and Fe II, and consequently the excitation to ionization ratio is highest for iron.

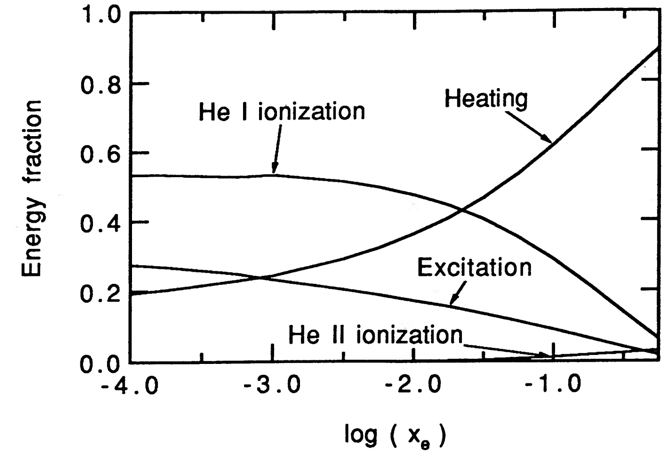

FIG. 3.—Energy fractions going into heating, excitation, and ionization for helium as a function of electron fraction.

Our results for O I can be compared to those of Dalgarno & Lejeune (1971), who studied a weakly ionized gas, with x_e in the range 10^{-6} to 10^{-2}. The discrete nature of excitations and ionizations were taken into account, and approximately the same levels of O I as in this paper were included, as well as a separate treatment of the ionization to the three lowest states of O II. The injected electrons, however, had a maximum energy of only 100 eV, which makes a direct comparison with our results difficult. For this reason we have redone a calculation with initial energy 80 eV, for $x_e = 10^{-4}$, 10^{-3}, and 10^{-2}. From the calculations we find that the energy fraction going into heating, as well as the effective ionization potentials, found by Dalgarno & Lejeune differ by less than ~5% from what we find over this range in x_e. While the total fraction going into excitation is nearly the same, Dalgarno & Lejeune find that most of these excitations go into the 3s ^3S level, while we find that a substantial amount of the energy also goes into higher levels. At $x_e = 10^{-2}$ Dalgarno & Lejeune find that 8.6% of the

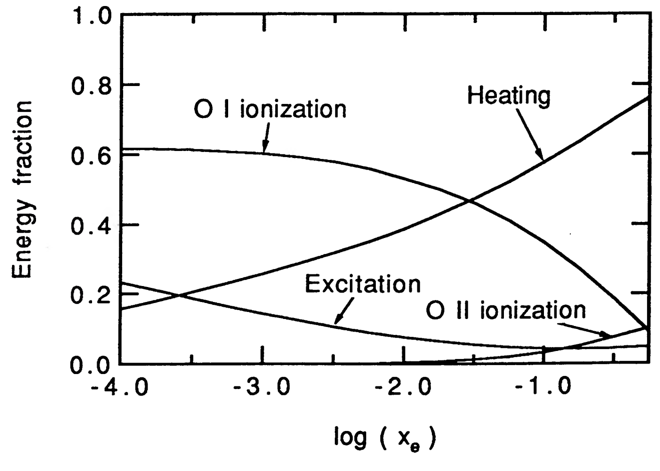

FIG. 4.—Same as Fig. 3 for oxygen

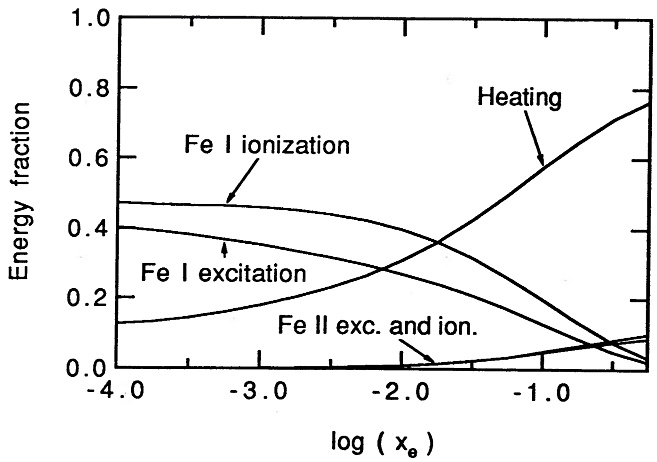

FIG. 5.—Same as Fig. 3 for iron. For Fe II the upper curve gives the ionization fraction and the slightly lower excitation fraction.

energy goes into this level, while we find only 2.5%. Presumably the difference is due to the cross section of the 3*s* ^3S level used by Dalgarno & Lejeune, which is a factor of 2.5 larger than our value, taken from Laher & Gilmore (1990).

Peterson & Green (1968) have made calculations for He I, without, however, taking Coulomb heating into account. At $x_e = 10^{-4}$ and 3 keV Peterson & Green find that $\chi_{\rm eff} = 46.2$ eV, while we find 45.9 eV. The heating contribution at this x_e is however, 19.4%, so a real comparison is difficult.

Because of its great importance for Type Ia supernovae we present detailed results of the excitation of Fe I and Fe II in Table 1. For Fe I we only include allowed transitions, since their cross sections are much larger than those of the forbidden. Excitations to these are therefore negligible, as is directly confirmed for Fe II, where both allowed and forbidden transitions are included. In Fe I nearly all excitations go to the quintet levels, while the triplet levels only receives a minor fraction. The same trend is seen for Fe II, where the $z\,^6D$, $z\,^6F$, and $z\,^6P$ multiplets dominate completely. Less than ~7% (for $x_e > 10^{-3}$) of the excitation energy of Fe II goes into metastable states. Excitations from the first excited level, $a\,^4F$, to higher levels are also unimportant compared to those from the ground state.

It should be pointed out that our results for the excitation are based on the Bethe approximation for the cross sections for Fe I and Fe II, and may therefore be less accurate than for other ions. For Fe I and Fe II no other calculations are known, except for Axelrod (1980), who makes some rough estimates based on the sum of the oscillator strengths, which differ substantially from our results. Axelrod finds for Fe II, by adding the oscillator strengths, that only 4% of the energy of the primaries goes into excitation, while we find that ~50% of the energy goes into excitation at $x_e = 10^{-2}$. The main reason for this difference seems to be that Axelrod did not include secondary electrons in his calculations, which pile up at lower energies, where excitations are comparatively more important, $\sigma_{\rm exc} \propto f(\ln E/E)$ (see Figs. 1 and 2 for oxygen). When calculating the loss function it is also somewhat misleading to use the sum $\sum_i f_{1j}$, since $dE/dx \propto \sum_j f_{1j} \ln E_{1j}$. This weighting increases the energy going into ionization compared to excitation. This example illustrates the importance of a real solution of the Boltzmann equation, rather than analytical approximations. Because of the similar atomic structure of Fe I–II, Co I–II, and Ni I–II our results for Fe I–II should also be applicable to these ions.

3.3. *Electron Thermalization in Core Collapse Supernovae*

Stars more massive than ~10 $M_\odot$ end their lives as core collapse supernovae. Explosive nucleosynthesis behind the

TABLE 1

ENERGY FRACTIONS GOING INTO EXCITATION OF THE FE I AND FE II MULTIPLETS

	x_e					
LOWER AND UPPER LEVELS	$10^{-0.5}$	$10^{-1.0}$	$10^{-1.5}$	$10^{-2.0}$	$10^{-2.5}$	$10^{-3.0}$
Fe I:						
$a\,^5D$–$z\,^5D$	3.80–03[a]	9.91–03	1.64–02	2.18–02	2.64–02	3.09–02
$a\,^5D$–$z\,^5F$	7.18–03	1.87–02	3.08–02	4.07–02	4.90–02	5.67–02
$a\,^5D$–$z\,^5P$	3.40–03	8.82–03	1.45–02	1.90–02	2.25–02	2.56–02
$a\,^5D$–$z\,^5G$	2.72–04	7.03–04	1.14–03	1.46–03	1.69–03	1.85–03
$a\,^5D$–$y\,^5D$	1.44–02	3.71–02	6.01–02	7.78–02	9.05–02	1.00–01
$a\,^5D$–$y\,^5F$	8.84–03	2.28–02	3.68–02	4.76–02	5.52–02	6.09–02
$a\,^5D$–$y\,^5P$	9.59–03	2.47–02	3.98–02	5.09–02	5.84–02	6.35–02
$a\,^5D$–$n\,^3L$[b]	2.00–03	5.15–03	8.33–03	1.07–02	1.25–02	1.37–02
Total	4.95–02	1.28–01	2.08–01	2.70–01	3.16–01	3.53–01
Fe II:						
$a\,^6D$–$z\,^6D$	1.70–02	1.06–02	5.17–03	2.17–03	8.53–04	3.26–04
$a\,^6D$–$z\,^6F$	3.54–02	2.20–02	1.07–02	4.42–03	1.71–03	6.37–04
$a\,^6D$–$z\,^6P$	1.54–02	9.57–03	4.63–03	1.92–03	7.38–04	2.73–04
$a\,^6D$–$n\,^2L$, $n\,^4L$[c]	7.80–04	4.84–04	2.33–04	9.58–05	3.66–05	1.34–05
$a\,^4F$–$n\,^2L$, $n\,^4L$, $n\,^6L$[d]	6.20–03	3.86–03	1.88–03	7.82–04	3.05–04	1.15–04
$a\,^6D$–metastable	8.14–04	6.48–04	4.58–04	3.03–04	1.96–04	1.26–04
Total	7.56–02	4.72–02	2.30–02	9.68–03	3.84–03	1.49–03

[a] Our notation is such that, e.g., 3.80–03 denotes 3.80×10^{-3}.

[b] Excitation from $a\,^5D$ to the triplet levels, $z\,^3F$, $z\,^3D$, $z\,^3P$, $z\,^3G$, $y\,^3F$, $y\,^3D$.

[c] Excitation from $a\,^6D$ to the multiplets $z\,^4F$, $z\,^4D$, $z\,^4P$, and $c\,^2F$.

[d] Excitation from the excited level $a\,^4F$ to $z\,^6D$, $z\,^6F$, $z\,^6P$, $z\,^4F$, $z\,^4D$, $z\,^4P$, and $c\,^2F$.

shock burns the innermost parts to nearly nuclear statistical equilibrium, and most of the mass is turned into ^{56}Ni. Outside the iron core, explosive oxygen burning results in silicon, sulphur, argon, and calcium in a thin shell. Further out, no explosive nucleosynthesis occurs, and the composition is the same as in the presupernova. Presupernova models and explosive nucleosynthesis have been calculated for various masses by Woosley & Weaver (1986), and specifically for SN 1987A by Woosley (1988), Shigeyama, Nomoto, & Hashimoto (1988), and Hashimoto, Nomoto, & Shigeyama (1989). Differences between these SN 1987A presupernova models, which also illustrate the uncertainties involved, are discussed by Nomoto & Hashimoto (1988).

We have calculated the energy deposition for a number of compositions characteristic of core collapse supernovae. Here we mainly discuss the results for compositions taken from the 10H model by Woosley (1988). For each shell we determine the abundances at a representative mass point in the shell, given in Table 2. As a comparison we have made calculations for the 11E1 model by Shigeyama et al. (1988). The resulting differences are discussed in § 3.3.6 below. For the hydrogen envelope we assume solar abundances from Allen (1973). All calculations are done for electron fractions in the range 10^{-4} to $10^{-0.5}$. We assume that the ionized fraction of an element is proportional to the electron fraction, except for sodium and calcium, which for reasons discussed in § 4 are assumed to be mainly ionized, as long as the total electron fraction is higher than the total abundances of these elements. In the silicon-calcium shell the calcium abundance is $\sim 2.6 \times 10^{-2}$, and we therefore require the fraction of Ca II not to exceed x_e.

To make the results easily accessible to other users, we have fitted the effective ionization potentials of the elements to an expression of the form

$$\chi_{\rm eff}(x_e) = C \times 10^{\alpha} \,, \tag{14}$$

where

$$\alpha = \sum_{i=1}^{4} a_i [\log_{10}(x_e) + 4]^i \,. \tag{15}$$

The same expression is used for the total fractions going into heating, excitation, and ionization. The fits should only be used in the interval $x_e = 10^{-4}$ to $10^{-0.5}$. The parameters C and a_i are given in Table 2. C has the convenient interpretation of being the effective ionization potential, respectively the energy fraction, at $x_e = 10^{-4}$. In Table 3 we give for each composition the most important levels of excitation for $x_e = 10^{-2}$. For other values of x_e these can to a good approximation be scaled by the total fraction going into excitations of the various ions.

The effective ionization potentials given in Table 2 can be used for other similar compositions, not differing substantially from those in Table 2, as long as one takes care of energy conservation. This means that the sum of all fractions going into the different channels should be equal to one,

$$\eta_h + \sum_i \sum_n \eta_{in} + \sum_i \eta_{ic} = 1 \,, \tag{16}$$

where the energy fraction going into ionization of an element i can be written as (eq. [12])

$$\eta_{ic} = \frac{I_i}{\chi_{{\rm eff},i}(x_e)} X_i \,. \tag{17}$$

Similar scaling laws can be used for the excitations. Equation (16) is fulfilled for the results in Table 2. If used for a different

TABLE 2

PARAMETERS DESCRIBING THE ELECTRON THERMALIZATION IN EACH COMPOSITION ZONE[a]

Ion	Abundances[b]	C(eV)	a_1	a_2	a_3	a_4
		A. Hydrogen Envelope (Solar Abundances)				
H I	0.92+00	32.81	−0.1383−01	0.3011−01	−0.1607−01	0.5735−02
He I	0.77−01	42.76	−0.1292−01	0.3014−01	−0.2300−01	0.7044−02
He II	...	264.9	−0.1652−01	0.3996−01	−0.2963−01	0.8020−02
C I	0.41−03	8.50	−0.1294−01	0.3135−01	−0.1878−01	0.6176−02
C II	...	36.64	−0.3969−02	0.1833−01	−0.1636−01	0.6137−02
N I	0.11−03	10.57	−0.1215−01	0.2890−01	−0.2033−01	0.6551−02
N II	...	35.40	−0.1136−01	0.3089−01	−0.2398−01	0.7231−02
O I	0.80−03	10.59	−0.1167−01	0.3196−01	−0.2269−01	0.6902−02
O II	...	33.88	−0.1315−01	0.3242−01	−0.2551−01	0.7473−02
Ne I	0.10−03	16.71	−0.1029−01	0.3182−01	−0.2555−01	0.7464−02
Na I	0.27−06	1.69	0.4172+00	−0.1402+00	0.2547−01	0.1318−02
Na II	...	38.55	−0.1456−01	0.4160−01	−0.3102−01	0.8155−02
Mg I	0.33−04	3.18	0.2266+00	−0.3135−01	0.4768−02	0.2542−02
Mg II	...	29.11	−0.1766−01	0.3944−01	−0.2315−01	0.6644−02
Si I	0.41−04	3.17	0.2028+00	−0.3949−01	0.5850−02	0.2772−02
Si II	...	19.63	−0.5790−02	0.1466−01	−0.8207−02	0.4630−02
S I	0.20−04	5.16	−0.1471−01	0.4221−01	−0.2192−01	0.6415−02
S II	...	20.99	−0.3658−02	0.1299−01	−0.1170−01	0.5381−02
Ar I	0.86−05	6.69	0.1484−03	0.1705−01	−0.1432−01	0.5806−02
Ca I	0.24−05	2.02	0.2018+00	−0.3944−01	−0.1137−02	0.4134−02
Ca II	...	11.51	−0.1092−01	0.2889−01	−0.1743−01	0.6007−02
Fe I	0.49−04	8.44	0.1011+00	0.2084−01	−0.1181−01	0.4609−02
Fe II	...	15.52	−0.1316−01	0.2725−01	−0.1729−01	0.6007−02
Heat		0.126	0.1153+00	0.1710−01	0.1927−01	−0.4129−02
Excitation		0.445	0.3202−01	−0.1461+00	0.8186−01	−0.1753−01
Ionization		0.426	0.4541−01	−0.9108−01	0.5402−01	−0.1321−01

TABLE 2—*Continued*

Ion	Abundances[b]	C(eV)	a_1	a_2	a_3	a_4
			B. The Helium-Nitrogen Zone			
He I	0.996+00	45.71	−0.1843−01	0.3903−01	−0.1977−01	0.5727−02
He II	...	325.8	−0.3181−01	0.5119−01	−0.3036−01	0.7484−02
C I	0.90−04	4.93	0.1686+00	−0.5371−02	−0.1167−01	0.4847−02
C II	...	33.88	0.2883−01	−0.8314−03	−0.1068−02	0.3164−02
N I	0.35−02	8.06	0.8656−01	0.1406−01	−0.1578−01	0.5325−02
N II	...	38.90	−0.1071−01	0.2593−01	−0.1555−01	0.5327−02
O I	0.59−04	8.57	0.7841−01	0.1712−01	−0.1807−01	0.5693−02
O II	...	39.26	−0.2807−01	0.4197−01	−0.2343−01	0.6422−02
Ne I	0.34−03	19.19	−0.2534−01	0.4541−01	−0.2494−01	0.6547−02
Na I	0.98−06	0.42	0.7070+00	−0.9092−01	−0.1127−01	0.5328−02
Na II	...	50.12	−0.4230−01	0.6083−01	−0.3493−01	0.8036−02
Mg I	0.12−03	0.56	0.6648+00	−0.6981−01	−0.4182−02	0.3282−02
Mg II	...	19.28	0.1146+00	0.3951−01	−0.2949−01	0.6956−02
Si I	0.99−04	0.62	0.6641+00	−0.1317+00	0.2000−01	0.4722−03
Si II	...	10.02	0.1654+00	−0.4494−02	−0.4434−02	0.3398−02
S I	0.50−04	2.18	0.3464+00	−0.1002+00	0.1551−01	0.1778−02
S II	...	16.98	0.4412−01	0.1646−02	0.4684−03	0.2686−02
Ar I	0.12−04	4.78	0.1038+00	−0.2059−01	0.4196−02	0.2485−02
Ca I	0.74−05	0.49	0.6460+00	−0.1243+00	0.2966−02	0.3942−02
Ca II	...	6.64	0.1994+00	−0.5148−01	0.8458−02	0.2216−02
Heat		0.183	0.8572−01	0.1476−01	0.1253−01	−0.2529−02
Excitation		0.269	−0.2928−02	−0.1083+00	0.5417−01	−0.1182−01
Ionization		0.544	0.2403−01	−0.6026−01	0.3468−01	−0.8962−02
			C. The Helium-Carbon Zone			
He I	0.98+00	47.10	−0.1060−01	0.2990−01	−0.1662−01	0.5337−02
He II	...	330.4	−0.1706−01	0.3819−01	−0.2600−01	0.6945−02
C I	0.18−01	5.92	0.7765−01	0.3947−01	−0.2156−01	0.5624−02
C II	...	36.31	−0.7076−02	0.2845−01	−0.1139−01	0.4384−02
N I	0.69−05	9.11	0.3021−01	0.4428−01	−0.2343−01	0.6029−02
N II	...	40.09	−0.7666−02	0.2268−01	−0.1469−01	0.5219−02
O I	0.20−02	9.64	0.2264−01	0.4801−01	−0.2600−01	0.6425−02
O II	...	39.99	−0.1288−01	0.2807−01	−0.1879−01	0.5859−02
Ne I	0.40−02	19.59	−0.1178−01	0.3218−01	−0.2045−01	0.5997−02
Na I	0.10−05	0.75	0.3263+00	0.1448+00	−0.7622−01	0.1189−01
Na II	...	50.70	−0.2406−01	0.4471−01	−0.2941−01	0.7350−02
Mg I	0.13−03	1.02	0.2787+00	0.1669+00	−0.6984−01	0.1002−01
Mg II	...	22.54	0.4814−01	0.6605−01	−0.3362−01	0.7096−02
Si I	0.10−03	1.11	0.2539+00	0.1519+00	−0.6845−01	0.1050−01
Si II	...	12.33	0.4088−01	0.7718−01	−0.2891−01	0.6055−02
S I	0.52−04	3.02	0.1181+00	0.5546−01	−0.3107−01	0.6792−02
S II	...	18.62	−0.7619−02	0.4196−01	−0.1341−01	0.4319−02
Ar I	0.13−04	5.50	0.1163−01	0.4952−01	−0.1907−01	0.5174−02
Ca I	0.77−05	0.84	0.2724+00	0.1209+00	−0.6886−01	0.1162−01
Ca II	...	8.24	0.5001−01	0.5410−01	−0.2417−01	0.5796−02
Heat		0.140	0.2482+00	−0.7192−01	0.3316−01	−0.4363−02
Excitation		0.303	−0.4911−01	−0.9768−01	0.5434−01	−0.1203−01
Ionization		0.552	0.1571−01	−0.5400−01	0.3242−01	−0.8629−02
			D. The Oxygen-Carbon Zone			
C I	0.16+00	16.90	−0.6885−02	0.2153−01	−0.6086−02	0.2837−02
C II	...	81.28	−0.3409−02	0.1217−01	−0.8530−02	0.3713−02
O I	0.82+00	23.77	−0.1218−01	0.2839−01	−0.1416−01	0.4127−02
O II	...	85.11	−0.1226−01	0.2862−01	−0.2040−01	0.5381−02
Ne I	0.16−01	42.17	−0.1399−01	0.3018−01	−0.2025−01	0.5257−02
Na I	0.62−05	2.88	0.9358−01	0.1061+00	−0.2757−01	0.3771−02
Na II	...	106.2	−0.2109−01	0.4352−01	−0.2822−01	0.6283−02
Mg I	0.76−03	4.66	0.4506−01	0.7582−01	−0.6229−03	−0.2527−03
Mg II	...	62.23	−0.1174−01	0.2854−01	−0.9996−02	0.3183−02
Si I	0.38−03	4.91	0.2953−01	0.7092−01	−0.4206−02	0.7223−03
Si II	...	35.81	−0.4084−02	0.1207−01	0.1285−02	0.1849−02
S I	0.19−03	9.58	−0.8363−02	0.3595−01	−0.8744−02	0.2829−02
S II	...	43.45	−0.1884−02	0.8269−02	−0.3913−02	0.2962−02
Ar I	0.46−04	13.61	−0.4663−02	0.1368−01	−0.4912−02	0.2993−02
Ca I	0.28−04	3.24	0.5320−01	0.8277−01	−0.2158−01	0.3567−02
Ca II	...	22.39	−0.5441−03	0.1661−01	−0.4288−02	0.2668−02
Heat		0.121	0.3199+00	−0.7042−01	0.1903−01	−0.2063−02
Excitation		0.281	−0.1618+00	0.3118−01	−0.4824−01	0.9615−02
Ionization		0.593	0.8046−02	−0.2335−01	0.1137−01	−0.3890−02

TABLE 2—*Continued*

Ion	Abundances[b]	C(eV)	a_1	a_2	a_3	a_4
			E. The Oxygen-Silicon-Sulphur Zone			
C I	0.17−01	17.95	−0.5712−02	0.1636−01	−0.5790−02	0.3010−02
C II	...	83.75	−0.4711−02	0.1429−01	−0.1054−01	0.4094−02
O I	0.85+00	24.66	−0.1325−01	0.2855−01	−0.1552−01	0.4456−02
O II	...	86.10	−0.1404−01	0.3137−01	−0.2198−01	0.5650−02
Ne I	0.93−02	42.76	−0.1500−01	0.3207−01	−0.2163−01	0.5516−02
Na I	0.91−04	3.67	0.5338−01	0.9721−01	−0.2212−01	0.3217−02
Na II	...	106.4	−0.2238−01	0.4567−01	−0.2935−01	0.6482−02
Mg I	0.11−01	5.88	0.1863−01	0.6159−01	0.4765−02	−0.6498−03
Mg II	...	65.61	−0.1008−01	0.2300−01	−0.9467−02	0.3329−02
Si I	0.65−01	6.03	0.1159−01	0.5411−01	0.1721−02	0.2654−03
Si II	...	38.46	−0.2547−02	0.7454−02	0.7797−03	0.2171−02
S I	0.39−01	10.40	−0.9098−02	0.2793−01	−0.7303−02	0.2887−02
S II	...	45.29	−0.2169−02	0.8803−02	−0.5712−02	0.3360−02
Ar I	0.53−02	14.29	−0.4906−02	0.1341−01	−0.6545−02	0.3388−02
Ca I	0.55−03	3.97	0.2240−01	0.7385−01	−0.1687−01	0.3121−02
Ca II	...	23.93	−0.5327−02	0.1594−01	−0.5384−02	0.2991−02
Fe I	0.30−07	15.03	0.3289−02	0.5041−01	0.2273−02	0.2010−03
Fe II	...	33.50	−0.4871−02	0.1380−01	−0.6410−02	0.3228−02
Heat		0.125	0.2783+00	−0.4872−01	0.1477−01	−0.1795−02
Excitation		0.237	−0.1566+00	0.3428−01	−0.3946−01	0.7850−02
Ionization		0.634	0.7393−02	−0.3328−01	0.1445−01	−0.4152−02
			F. The Silicon-Calcium Zone			
C I	0.38−05	24.83	−0.1444−01	0.3291−01	−0.2325−01	0.5954−02
C II	...	105.0	−0.1651−01	0.3715−01	−0.2629−01	0.6405−02
O I	0.94−04	30.48	−0.2055−01	0.4235−01	−0.2790−01	0.6448−02
O II	...	95.72	−0.2419−01	0.4927−01	−0.3207−01	0.7017−02
Ne I	0.12−08	47.53	−0.2371−01	0.4838−01	−0.3151−01	0.6908−02
Na I	0.11−06	9.80	−0.6866−02	0.6306−01	−0.2413−01	0.5248−02
Na II	...	110.4	−0.2736−01	0.5347−01	−0.3365−01	0.7057−02
Mg I	0.13−04	16.37	0.2780−02	0.1007−01	0.1362−02	0.2047−02
Mg II	...	84.92	−0.1125−01	0.2695−01	−0.1983−01	0.5255−02
Si I	0.63+00	14.93	0.1020−02	0.1119−01	−0.3194−02	0.2909−02
Si II	...	57.54	−0.1220−01	0.2988−01	−0.2188−01	0.5958−02
S I	0.29+00	15.52	−0.1370−01	0.3118−01	−0.2138−01	0.5638−02
S II	...	60.26	−0.1614−01	0.3661−01	−0.2588−01	0.6428−02
Ar I	0.41−01	19.50	−0.1607−01	0.3625−01	−0.2546−01	0.6366−02
Ca I	0.26−01	8.85	−0.1034−01	0.4101−01	−0.1893−01	0.4919−02
Ca II	...	33.65	−0.1499−01	0.3407−01	−0.2373−01	0.6052−02
Fe I	0.12−01	35.08	−0.5525−02	0.1611−01	−0.6897−02	0.3489−02
Fe II	...	44.67	−0.1493−01	0.3394−01	−0.2386−01	0.6024−02
Heat		0.088	0.3469+00	−0.9228−01	0.3170−01	−0.3805−02
Excitation		0.322	−0.1161+00	0.2963−02	−0.8325−02	0.1863−02
Ionization		0.591	0.1164−01	−0.3290−01	0.1888−01	−0.5683−02
			G. The Iron Zone			
He I	0.56+00	49.20	−0.5616−02	0.2013−01	−0.1804−01	0.6516−02
He II	...	311.9	−0.8702−02	0.3050−01	−0.2551−01	0.7624−02
C I	0.28−03	9.69	−0.1477−03	0.9677−02	−0.8974−02	0.5074−02
C II	...	41.40	0.2568−02	0.6712−02	−0.1013−01	0.5417−02
O I	0.39−06	12.25	−0.7145−02	0.2254−01	−0.1781−01	0.6384−02
O II	...	39.26	−0.9599−02	0.2710−01	−0.2235−01	0.7152−02
Ne I	0.48−06	19.54	−0.8697−02	0.2654−01	−0.2226−01	0.7122−02
Na I	0.77−08	3.91	0.1417−01	0.4473−01	−0.1143−01	0.4288−02
Na II	...	46.45	−0.1286−01	0.3659−01	−0.2867−01	0.8008−02
Mg I	0.94−06	6.08	0.9207−02	0.1434−01	0.9677−02	0.1097−02
Mg II	...	34.04	−0.3504−02	0.1509−01	−0.1229−01	0.5402−02
Si I	0.11−04	5.54	0.5863−02	0.1177−01	0.6210−02	0.1977−02
Si II	...	21.88	0.7705−02	−0.3531−02	−0.7791−03	0.3948−02
S I	0.34−04	6.03	−0.2592−02	0.1363−01	−0.9035−02	0.4944−02
S II	...	23.44	0.3918−02	0.3420−02	−0.7186−02	0.4976−02
Ar I	0.55−04	7.55	0.2427−02	0.5861−02	−0.7965−02	0.5087−02
Ca I	0.19−03	3.42	0.4350−02	0.2777−01	−0.7524−02	0.4130−02
Ca II	...	13.06	0.9099−03	0.8544−02	−0.8160−02	0.4978−02
Fe I	0.44+00	13.06	−0.2592−02	0.1771−01	0.1755−02	0.2686−02
Fe II	...	17.54	0.1127−02	0.8353−02	−0.9045−02	0.5122−02
Heat		0.105	0.1742+00	0.2427−01	0.9469−02	−0.3020−02
Excitation		0.348	−0.6614−01	0.6591−02	−0.8752−02	−0.6298−03
Ionization		0.546	0.1591−02	−0.1534−01	0.6418−02	−0.4119−02

[a] Coefficients C and a_i to the analytic fits to the effective ionization potentials, and the total fraction going into heating, excitation, and ionization (eqs. [14] and [15]).

[b] Total abundances by number for each element. The ionized fraction is proportional to the electron fraction, except for sodium and calcium which are assumed to be mainly ionized.

TABLE 3

NONTHERMAL EXCITATIONS

Solar Abundances	He–N Zone	He–C Zone	O–C Zone	O–Si–S Zone	Si–Ca Zone	Fe–He Zone
H I $2p$ (74.2%)[a]	He I $2p$ $^1P^o$ (66.1%)	He I $2p$ $^1P^o$ (63.2%)	C I $3p$ (16.0%)	O I $3s$ $^3S^o$ (14.3%)	Si I $4s$ $^3P^o$ (22.3%)	He I $2p$ $^1P^o$ (26.4%)
$3p$ (10.8%)	$3p$ $^1P^o$ (16.2%)	$3p$ $^1P^o$ (15.5%)	$3d$ (6.8%)	$3s'$ $^3D^o$ (11.9%)	$4d$ $^3D^o$ (16.8%)	$3p$ $^1P^o$ (6.4%)
$2s$ (5.9%)	$2s$ ^1S (6.1%)	$2s$ ^1S (5.8%)	$3s$ (6.4%)	$4p$ ^3P (6.1%)	$3d$ $^3D^o$ (8.3%)	$2s$ ^1S (1.9%)
$3d$ (1.7%)	$2s$ ^3S (3.2%)	$2s$ ^3S (3.0%)	$4p$ (4.1%)	$3d$ $^3D^o$ (4.9%)	$3d$ $^3P^o$ (3.6%)	Fe I y ^5D (17.1%)
$4p$ (1.6%)	$2p$ $^3P^o$ (2.4%)	$2p$ $^3P^o$ (2.3%)	$4d$ (3.3%)	$3p$ ^3P (4.4%)	$3p$ ^1D (3.4%)	y ^5P (11.3%)
$3s$ (1.0%)	$3s$ ^1S (1.5%)	$3s$ ^1S (1.4%)	$2p$ ^1D (1.9%)	$4s$ $^3S^o$ (3.0%)	S I $3d$ $^3D^o$ (10.0%)	z ^5D (4.8%)
He I $2p$ $^1P^o$ (3.0%)	$3d$ ^1D (1.0%)	$3d$ ^1D (1.0%)	$5d$ (1.7%)	$2p$ ^1D (2.9%)	$4s''$ $^3P^o$ (7.0%)	z ^5F (9.2%)
	$3s$ ^3S (1.0%)	$3s$ ^3S (1.0%)	$4s$ (1.7%)	$4d$ $^3D^o$ (2.8%)	$4s$ $^3S^o$ (5.5%)	z ^5D (4.8%)
	$3p$ $^3P^o$ (1.0%)	$3p$ $^3P^o$ (1.0%)	O I $3s$ $^3S^o$ (14.2%)	$2p$ ^1S (0.9%)	$4s'$ $^3D^o$ (4.6%)	z ^5P (4.3%)
		C I $3p$ (1.7%)	$3s'$ $^3D^o$ (11.7%)	C I $3p$ (1.6%)	$6s$ $^3S^o$ (1.2%)	z ^3P (1.2%)
			$4p$ ^3P (6.2%)	Mg I $3p$ $^1P^o$ (13.4%)	Ar I $4s$ $^1P^o$ (1.2%)	
			$3d$ $^3D^o$ (4.9%)	Si I $4s$ $^3P^o$ (6.0%)	Ca I $4p$ $^1P^o$ (8.4%)	
			$3p$ ^3P (4.6%)	$4d$ $^3D^o$ (4.4%)	Ca II $4p$ $^2P^o$ (4.0%)	
			$2p$ ^1D (2.9%)	$3d$ $^3D^o$ (2.2%)		
			$4s$ $^3S^o$ (2.9%)	$3d$ $^3P^o$ (1.0%)		
			$4d$ $^3D^o$ (2.7%)	S I $3d$ $^3D^o$ (3.2%)		
			$2p$ ^1S (1.0%)	$4s''$ $^3P^o$ (2.2%)		
				$4s$ $^3S^o$ (1.9%)		
				$4s'$ $^3D^o$ (1.5%)		

[a] The percentage of the total excitation fraction going into excitation of a level at $x_e = 10^{-2}$. Only levels into which more than 1% of the total excitation energy is deposited are included.

composition this will in general not be true. As a first approximation the results can, however, be renormalized so that energy conservation is preserved.

For a given x_e, the energy going into the different channels depend on the composition of the plasma. If there is one dominating element in the plasma, as in the helium and oxygen zones, most of the excitation and ionization goes into this element. If there are several abundant elements, as in the hydrogen envelope and the iron-helium core, the relative abundances are important. This can be seen from a comparison of our results with similar calculations by Shull & Van Steenberg (1985) and Xu & McCray (1991b), having different hydrogen and helium abundances (§ 3.3.1), and for the iron-helium cores in the 10H and 11E1 models (§ 3.3.6). The dependence on the composition increases with decreasing electron fraction, because excitation and ionization are then more important. After these general remarks we now discuss the deposition zone by zone.

3.3.1. *The Hydrogen Envelope*

The nonthermal energy deposition in a gas of solar abundance is of interest not only for the supernova envelope, but also for objects like the emission-line regions of active galactic nuclei. In this paper we use solar abundances with 92% hydrogen, and 7% helium, and include heavier elements with abundances from Allen (1973). As described in the Appendix, we take into account excitations to all angular momentum levels up to $n = 4$ for H I (in total nine excited levels), and for He I all singlet and triplet levels with $n \leq 3$ (10 levels). The results are given in Tables 2A and 3. The major part of the energy going into excitation goes into hydrogen. At $x_e = 10^{-2}$ 5.4% of the total energy goes into excitation and ionization of helium. By far the most dominating excitation level is the H I $2p$ (1215.7 Å) resonance level (23.3% at $x_e = 10^{-2}$). After this the most important H I levels are $3p$, $2s$, and $3d$. For He I most energy goes into excitation of the $2p$ ^1P level. Less than 0.3% of the deposited energy goes into excitation and ionization of the heavy elements. A lower total metal abundance in the hydrogen envelope, like that appropriate for SN 1987A, does not change the results appreciably. Because of CNO-processing and mixing, the helium abundance in the envelope may differ substantially from solar (e.g., Saio, Nomoto, & Kato 1988). To investigate the influence of a higher helium abundance, we have therefore made one calculation with a doubled helium abundance. While the total energy deposition into helium is nearly proportional to the helium abundance, the differences in the effective ionization potentials are less than ~0.5 eV.

Monte Carlo calculations for a hydrogen-helium mixture with 91% hydrogen and 9% helium by number, have been made by Shull & Van Steenberg (1985). The maximum electron energy in the calculations by Shull & Van Steenberg was 3 keV, the same as in this paper. The overall agreement with their results is good, taking the slightly different helium abundance into account. The main difference is that we find that less energy goes into heating and more energy into ionization, which probably reflects the lower helium abundance in our case. The differences are less than 4% and are within the statistical errors given by Shull & Van Steenberg. Shull & Van Steenberg included excitations only to the $n = 2$ level of H I. The effect of higher levels was simulated by multiplying the $n = 2$ cross section by a factor 1.35. To check this assumption we have done calculations with the same composition as Shull & Van Steenberg, both including all $n \leq 4$ levels for H I, and with only $n = 2$ plus their 1.35 factor. We find that the factor 1.35 overestimates the energy fraction going into excitation by up to 15%–20%.

Xu & McCray (1991b) calculated the deposition into pure hydrogen, including all levels up to $n = 10$, but lumping all l-levels together. They find substantially larger excitation rates than ours, especially to $n = 2$. At $x_e = 10^{-2}$ they find an energy fraction of 29.8%, while we find 25.2%. The reason for this difference, as they discuss, is mainly the neglect of helium in their calculations. The older cross sections from Johnson (1972) also give a slightly larger rate than ours from Callaway (1982), Callaway, Unnikrishnan, & Oza (1987), and Itikawa (1986) for the $2p$ level. In a test calculation with only hydrogen and using the same cross sections we find very good agreement with Xu & McCray. Our neglect of excitations to higher levels than $n = 4$ results in an underestimate of ~1% in the energy into excitations.

3.3.2. *The Helium Shell*

The helium zone can be divided into two distinct parts. In the outer, here referred to as the helium-nitrogen zone, nitrogen is the most abundant element after helium, while in the inner part, the helum-carbon zone, the second most abundant element is carbon. The results for the two cases are similar. For $x_e > 10^{-3}$, the fractions going into heating, excitation, and ionization differ by less than $\sim 1\%$ between the two compositions.

In Tables 2B and 2C one notices that the effective ionization potentials are very low for some of the elements, most notably Na I, Mg I, Si I, and Ca I. The reason is that the dominant element, helium, is difficult to ionize with its high ionization potential. Other elements with low thresholds and large cross sections therefore absorb a proportionally large fraction of the energy, which results in a low effective ionization potential (eq. [12]). The difference in composition between the carbon-rich and nitrogen-rich zones has little influence on the effective ionization potentials. The effective ionization potential for He I is ~ 2 eV higher than in a pure helium plasma.

Almost all of the excitation energy goes into He I in the two zones. This is in contrast to ordinary thermal excitation, where C I, Mg II, Ca II, and Fe II dominate the collisional excitation (Fransson & Chevalier 1989). The dominant He I levels are the resonance levels $2p\ {}^1P$ (584.3 Å) and $3p\ {}^1P$ (537.0 Å). As we will discuss in § 4, this emission will be converted into UV emission of C I and other metals.

3.3.3. *The Oxygen Shell*

The oxygen fraction throughout this zone is $\sim 84\%$. Also here the zone may be divided into two regions. In the 10H model the outer 0.5 $M_\odot$, the oxygen-carbon zone, contains $\sim 16\%$ carbon and $\sim 2\%$ neon. This zone is a result of the helium-burning stage and has not been affected by explosive nucleosynthesis. The inner 1.5 $M_\odot$, the oxygen-silicon-sulphur zone, contains $\sim 6\%$ silicon, $\sim 4\%$ sulphur, and $\sim 1\%$ magnesium, and has to a large extent been modified by explosive nucleosynthesis. Generally, elements heavier than magnesium are synthesized in the explosion, while lighter elements are produced in the presupernova evolution.

Comparing the effective ionization potentials for O I in the oxygen-carbon zone and the oxygen-silicon-sulphur zone we find that χ_{eff} is ~ 0.5 eV higher, for all x_e, in the oxygen-silicon-sulphur zone than in the oxygen-carbon zone. For a pure oxygen plasma χ_{eff} for O I is lowered by ~ 1.5 eV compared to the mixed case.

In the oxygen-carbon zone the energy going into excitation, as well as ionization, is dominated by O I and C I. The most populated levels for O I are $3s\ {}^3S$ (1302 Å) and $3s'\ {}^3D$. For C I the three dominating levels are $3p\ {}^3P$, $3s\ {}^3P$ (1656–1658 Å), and $3d\ {}^3P$ (1261–1262 Å).

In the oxygen-silicon-sulphur zone the excitation is dominated by O I, Mg I, and Si I. The most important levels for O I are $3s\ {}^3S$ (1302 Å), $3s'\ {}^3D$, and $4p\ {}^3P$. Two other important levels are the resonance levels Mg I $3p\ {}^1P$ (2852 Å) and Si I $4s\ {}^3P$ (2516 Å).

3.3.4. *The Silicon-Calcium Shell*

The silicon-calcium zone in the 10H model contains $\sim 63\%$ silicon, $\sim 29\%$ sulphur, $\sim 4\%$ argon, and $\sim 2.6\%$ calcium. Consequently, nearly all energy goes into silicon and sulphur. The excitation in this zone goes mainly into Si I, S I, and Ca I. For Si I the dominant levels are $4s\ {}^3P$ (2516 Å), $4d\ {}^3D$ (1850 Å), and $3d\ {}^3D$ (2216 Å). For S I the most important level is $3d\ {}^3D$ (1425 Å) and for Ca I $4p\ {}^1P$ (4226 Å). At x_e higher than $\sim 2 \times 10^{-2}$ calcium is mainly ionized, and the Ca II H and K lines account for $\sim 10\%$ of the total excitation.

3.3.5. *The Iron Shell*

The iron core contains in the 10H model $\sim 56\%$ helium and $\sim 44\%$ iron, by number. The helium results from the so-called alpha-rich freeze-out (Woosley, Arnett, & Clayton 1973). Of the energy going into ionization approximately half goes into helium and half into iron. The excitation is at low x_e dominated by Fe I, and above $x_e \sim 0.3$ by Fe II. The dominant level for He I is the $2p\ {}^1P$ level. As we discussed in § 3.2, at low x_e, when most of the iron is in Fe I, nearly all excitation goes to the quintet levels, while above $x_e = 0.3$ the sextet levels of Fe II dominate.

3.3.6. *Comparisons of Different Supernova Models*

By comparing our results for the 10H and the 11E1 models we can check the sensitivity of our results to the specific composition used. The differences in the total fractions going into heating, excitation, and ionization only amounts to a few percent between the corresponding zones. The largest difference is for the fraction going into excitation in the iron core, reflecting a difference in the helium-to-iron ratio of 56:44 and 76:24, in the 10H and 11E1 models, respectively. The differences are 10%–30% in the total fractions going into excitation, depending on the electron fraction. For other zones the total fractions differ by less than 6%. Differences in effective ionization potentials between the models are largest for ions with the lowest ionization potentials, Na I, Mg I, Si I, Ca I, and Fe I, at low x_e. For these, the effective ionization potential may vary by up to $\sim 30\%$ in zones where these ions act as trace constituents. This effect has already been discussed for the helium zone. In general, ions with higher ionization potentials than ~ 10 eV and/or large abundances vary by less than $\sim 6\%$. As long as the abundances do not depart dramatically from these models, the results should therefore be generally applicable.

4. LINE EMISSION AND IONIZATION

In previous sections we have calculated the rate of excitation and ionization, following the thermalization of the nonthermal electrons. In this section we discuss the subsequent degradation of the photons resulting from these processes, and their effects on the state of ionization.

The energy going into heating leads to collisional excitation of low excitation levels of neutral and singly ionized elements. This part of the energy mainly enters the thermal balance and only influences the state of ionization indirectly. Some of the most important collisionally excited lines are [O I] $\lambda\lambda$6300, 6364, Mg I] λ4571, Mg II λ2800, [Ca II] λ7300, and the optical Fe II lines. At late times IR and far-IR fine-structure lines dominate. This is discussed in more detail by Fransson & Chevalier (1989).

Photons resulting from recombinations and nonthermal excitations undergo a complicated series of steps in the degradation, which have important implications both for the state of ionization and for the excitation of, for example, the Hα line. We therefore need to discuss the fate of the recombination and excitation radiation in the different zones. Of particular importance is the UV radiation above 3.4 eV (3646 Å), since this can ionize hydrogen from the $n = 2$ level.

For an *unmixed* core with well-stratified shells, the luminosity from a shell, i, in a given wavelength interval can be written as

$$L_i = \epsilon_i(1 - e^{-\Delta\tau_{\gamma,i}})e^{-\tau_{\gamma,i}}L_\gamma\ , \tag{18}$$

1992ApJ...390..602K

TABLE 4

GAMMA-RAY OPTICAL DEPTHS FOR THE DIFFERENT COMPOSITION ZONES IN THE 10H MODEL AT 500 DAYS

Zone	$\Delta\tau_{\gamma,i}$ [a]	$\tau_{\gamma,i}$ [b]	$\Delta\tau_{\gamma m,i}$ [c]	ϵ_i [d]
H	0.39	0.78	...	0.41
He	0.33	0.45	0.40	0.36
O–C	0.12	0.33	0.11	0.27
O–Si–S	0.24	0.088	0.20	0.23
Si–Ca	0.054	0.034	0.045	0.27
Fe–He	0.034	0.0	0.025	0.02

[a] γ-ray optical depths of each individual shell in the unmixed case.

[b] Total γ-ray optical depth from the center to the shell.

[c] γ-ray optical depths of each composition zone for a uniformly mixed sphere.

[d] Fraction of deposited energy emerging as UV lines from the zone.

where ϵ_i is the fraction of the energy from the shell emitted in the wavelength interval, $\Delta\tau_{\gamma,i}$ the γ-ray optical depth of the shell, and $\tau_{\gamma,i}$ the total γ-ray depth from the ^{56}Co source to the shell. For the 10H model $\Delta\tau_{\gamma,i}$ and $\tau_{\gamma,i}$ are given in Table 4 at 500 days. For other epochs they scale as $\tau_\gamma \propto t^{-2}$. From observations, as well as hydrodynamical models, it is known that instabilities and mixing are important, which can change the one-dimensional results drastically (e.g., Woosley 1988; Shigeyama & Nomoto 1990; Hachisu et al. 1990; Fryxell, Müller, & Arnett 1991; Herant & Benz 1991). To simulate the effects of this, we assume that the mass of the different zones in the core is uniformly mixed in radius within an homogeneous sphere with radius corresponding to 2000 km s^{-1}. This is close to the expansion velocity of the metal lines in SN 1987A (e.g., Phillips & Williams 1991). The mixing is, however, not likely to be on a microscopic scale, since the diffusion time scale is long compared to the hydrodynamic (Fryxell et al. 1991). Instead, the structure more resembles a large number of blobs and fingers, each with the same composition as the original, unmixed shell, before mixing sets in. Fryxell et al. refers to this as macroscopic mixing. The γ-ray deposition in each of these blobs will then be the same as in the individual shells of the unmixed model. The total γ-ray optical depths of the various composition zones are just determined by the masses of the zones and are given as $\Delta\tau_{\gamma m,i}$ in Table 4. In this case $\tau_{\gamma,i}$ lose their meaning, and only the total γ-ray depth of the core, $\tau_{\gamma,\text{core}}$, is of interest. For a uniform density core consisting of only helium and heavier elements,

$$\tau_{\gamma,\text{core}} = 1.43\left(\frac{M_\text{core}}{4\ M_\odot}\right)\left(\frac{V_\text{core}}{2000\ \text{km s}^{-1}}\right)^{-2} t_\text{yr}^{-2}\ . \tag{19}$$

The uniform mixing has mainly the effect of changing the absolute values of $\Delta\tau_{\gamma,i}$, while the relative values of $\Delta\tau_{\gamma,i}/\Delta\tau_\text{tot}$ for the various composition zones are nearly unchanged. The reason is that in the one-dimensional models most of the core is moving at the same velocity in a shell. In the simple case of a thin shell and a sphere with the same velocity, this gives a factor of 3 difference in $\Delta\tau_{\gamma,i}$.

4.1. *Ionization in the Core*

The electron fraction is, beside the temperature, the main parameter characterizing the radiative emission, as well as collisional processes in the gas. We calculate x_e for each zone from

$$\frac{4\pi J_\gamma \sigma_{\gamma,i}}{\chi_{\text{eff},i}(x_e)}\, n_{0,i} = \alpha_i(T_e) n_e n_{+i} \tag{20}$$

and

$$n_e = \sum_i n_{+i}\ , \tag{21}$$

where $n_{0,i}$ and n_{+i} are the number fractions of the neutral and once ionized atoms of element i, respectively, and $\sigma_{\gamma,i}$ is the γ-ray cross section. The recombination rate, α_i, includes low-temperature dielectronic recombination (Nussbaumer & Storey 1983, 1986). The neglect of charge transfer in equation (20) is questionable for some elements, mainly the trace ions (e.g., Fransson & Chevalier 1989; Fransson 1991; Xu & McCray 1991a), and can be important in redistributing the ionization to ions with lower ionization potentials. Since recombination rates of these ions are different, also the total electron fraction is changed. Charge transfer rates are unfortunately scarce, but we discuss some of the possible effects below.

The mean intensity, J_γ, can be written as

$$J_\gamma = \frac{L_\gamma D_\gamma}{16\pi^2 R_\text{core}^2}\ , \tag{22}$$

where R_core is the core radius, L_γ the γ-luminosity due to radioactive decay of ^{56}Co, given by

$$L_\gamma = 1.27 \times 10^{42}\left(\frac{M_\text{Ni}}{0.1\ M_\odot}\right) e^{-t/111\text{d}}\ \text{ergs s}^{-1}\ , \tag{23}$$

and D_γ the γ-ray deposition function. For a central γ-ray source D_γ is given by

$$D_\gamma(x) = \frac{e^{-\tau_{\gamma,i}}}{x^2}\ , \tag{24}$$

where $x = r/R_\text{core}$. On the other extreme, for a γ-ray source mixed uniformly in radius throughout a constant density core, D_γ can be expressed as

$$D_\gamma(x) = \frac{3}{2\tau_{\gamma,\text{core}}} \int_{-1}^{1} \{1 - e^{-\tau_{\gamma,\text{core}}[\sqrt{1-x^2(1-\mu^2)} - x\mu]}\}\, d\mu\ . \tag{25}$$

If $\tau_{\gamma,\text{core}} \ll 1$,

$$D_\gamma(x) = \frac{3}{2}\left[1 + \frac{1-x^2}{2x}\ln\left(\frac{1+x}{|1-x|}\right)\right] \tag{26}$$

(Fransson & Chevalier 1989), while if $\tau_{\gamma,\text{core}} \gg 1$, D_γ is nearly constant throughout the core,

$$D_\gamma(x) = \frac{3}{\tau_{\gamma,\text{core}}}\ . \tag{27}$$

In Figure 6 D_γ is shown as a function of x for different values of $\tau_{\gamma,\text{core}}$.

The total number density is estimated from

$$n = \frac{3\ M_\text{core}}{4\pi R_\text{core}^3\ A m_p} = \frac{4.5 \times 10^9}{A}\left(\frac{M_\text{core}}{4\ M_\odot}\right)\left(\frac{V_\text{core}}{2000\ \text{km s}^{-1}}\right)^{-3} t_\text{yr}^{-3}\ \text{cm}^{-3}\ , \tag{28}$$

where A is the mean atomic weight and M_core the core mass.

For x_e in the range 10^{-2} to $10^{-0.5}$ the effective ionization potentials depend on x_e approximately as $\chi_\text{eff} \propto x_e^{0.18}$. If $x_e \ll 1$, x_e can then be expressed in the form

$$x_e = x_0 F^{0.46}\left(\frac{T}{5000\ \text{K}}\right)^{\alpha}\left(\frac{t}{300\ \text{d}}\right)^{0.46} e^{-t/242\text{d}}\ , \tag{29}$$

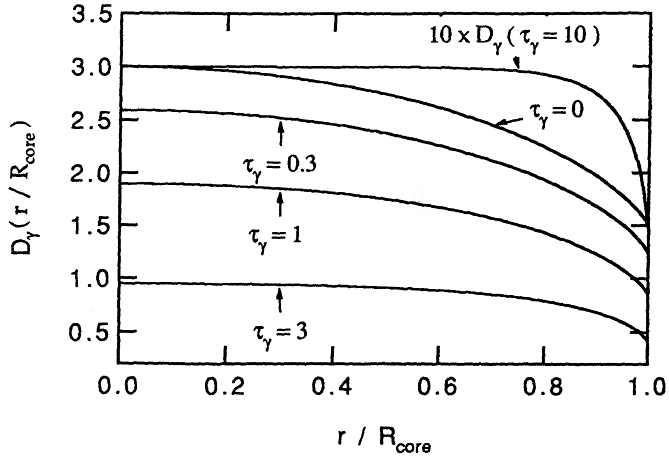

FIG. 6.—The γ-ray deposition function, D_γ, as a function of $x = r/R_{\text{core}}$, for different values of the γ-ray optical depth. Note that for $\tau_\gamma = 10$, D_γ is multiplied by a factor of 10.

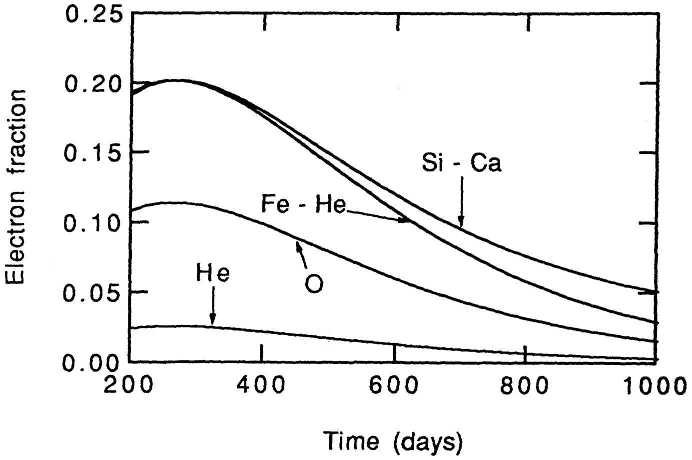

FIG. 7.—Electron fraction as a function of time for the different composition zones.

where

$$F = D_\gamma\left(\frac{V_{\text{core}}}{2000\ \text{km s}^{-1}}\right)\left(\frac{M}{4\ M_\odot}\right)^{-1}\left(\frac{M_{\text{Ni}}}{0.1\ M_\odot}\right) \tag{30}$$

is a parameter characterizing the core. We expect F to be of order unity, unless, for example, clumping is very important. The parameters x_0 and α are characteristic for the different regions and are given in Table 5. The temperature dependence, T^α, comes from the recombination coefficient of the dominant element in each region. In Figure 7 x_e is shown as a function of time for the different regions, assuming a uniformly mixed source. D_γ has been calculated for $r = 0.72R_{\text{core}}$, corresponding to the radius where most of the energy is emitted.

An important result is that the electron fraction is lower in the helium zone than in the other zones, due to the smaller mean atomic weight, as well as a higher effective ionization potential. In the helium and the oxygen zones electrons mainly come from the dominant element. In the iron core ∼98% of the electrons come from iron, even though there is a large abundance of helium. This result is a combination of the lower effective ionization potential, as well as recombination rate, for iron compared to helium, and the larger γ-ray cross section per atom for iron. In the silicon-calcium region, both silicon and sulphur contribute to the electron fraction. Argon and calcium also have fairly high abundances in this region. Of these, calcium is easily photoionized (see below) and contributes a fraction $X(\text{Ca}) \approx 0.03$ to x_e.

TABLE 5

PARAMETERS DESCRIBING THE ELECTRON FRACTION IN EQUATION (29)

Zone	x_0	α
He	0.082	0.32
O	0.47	0.32
Si–Ca	0.75	0.23
Fe–He	0.87	0.41

4.2. *Line Emission from the Core*

Nonthermal excitations and recombinations in each zone result in photons, which can ionize elements with low ionization potential. A case of special interest is hydrogen, which can be ionized from the $n = 2$ level. For this reason, we have estimated the fraction, ϵ_i, of the deposited energy emerging as photons with $h\nu > 3.4$ eV from each zone. In this calculation we include both the radiative cascades, resulting from recombinations, and nonthermal excitations. Collisional excitation by thermal electrons resulting in UV lines is, however, not included. An important case is Mg II λ2800 (see below and Fransson & Chevalier 1989).

In the helium zone, most of the nonthermal excitation goes to the $2s\ ^1S$ and $2p\ ^1P$ levels of helium. Electrons recombining to the triplets cascade to the $2s\ ^3S$ level, after which collisional transitions to the $2s\ ^1S$ or $2p\ ^1P$ levels occur (Osterbrock 1989). The $2p\ ^1P$–$1s\ ^1S$ transition results in λ584 Å photons which, in the absence of any destruction mechanisms, escape with a probability of

$$P_{\text{esc}} \sim \tau^{-1} = 4.8 \times 10^{-10}\left(\frac{M}{4\ M_\odot}\right)^{-1} \times \left(\frac{V_{\text{core}}}{2000\ \text{km s}^{-1}}\right)^3\left(\frac{t}{300\ \text{d}}\right)^2 . \tag{31}$$

Before escaping the 584 Å photons can, however, be destroyed by continuum absorption or by branching into the $2s\ ^1S$ level with the emission of a 2.08 μm photon. The probability of the latter is $P_{\text{branch}} \sim 1.1 \times 10^{-3}$. After helium, carbon is the most abundant element in the helium-carbon zone, with a number fraction of ∼2%, and continuum absorption is therefore dominated by C I, with a cross section of 7.2×10^{-18} cm^2 at 584 Å. The continuum destruction probability for a line has been calculated by Hummer & Rybicki (1985), and using their expression we find

$$P_{\text{cont}} \sim 4.9\beta \sim 7 \times 10^{-6}\left(\frac{T}{5000\ \text{K}}\right)^{0.5}\left[\frac{X(\text{C I})}{0.018}\right], \tag{32}$$

where $\beta \equiv \kappa_c/\kappa_l$ is the ratio of continuum to line opacity. This estimate is valid as long as $\beta \ll 1$ and $1 \ll \tau$. Therefore, $P_{\text{esc}} \ll$

$P_{\rm cont} \ll P_{\rm branch}$, and the 584 Å photons are recycled into a 2.08 μm $2p\ ^1P$–$2s\ ^1S$ photon, plus He I two-photon continuum emission with a total energy of 20.6 eV.

In the discussion above we have neglected collisional de-excitation of both the $2p\ ^1P$ and the $2s\ ^1S$ levels. At 200 days the ratios of the collisional de-excitation to radiative de-excitation for the $2p\ ^1P$–$1s\ ^1S$ transition is ~ 0.15 and for the $2s\ ^1S$–$1s\ ^1S$ transition ~ 0.01, decreasing rapidly with time. Therefore, both recombinations and nonthermal excitations end up in the $2s\ ^1S$ level, and a significant fraction of the energy emerges as two-photon emission. This could in principle ionize hydrogen. However, the continuum optical depth of C I within the helium zone is $\tau_c \sim 2.2 \times 10^6 (V_{\rm core}/2000\ {\rm km\ s^{-1}})^{-2} (t/300\ {\rm d})^{-2}$ at 11.26 eV, and the two-photon emission above 11.26 eV therefore instead ionizes carbon, resulting in C I recombination emission. From the two-photon distribution we find that 63% of the energy can ionize C I. From calculations of the C I recombination cascade by Escalante & Victor (1990), we estimate that $\sim 60\%$ of the energy in the recombination radiation of C I is above the Balmer limit. In addition, 35% of the energy emitted in the two-photon transition is in the range 3.4–11.26 eV. Therefore, in total $0.63 \times 0.60 + 0.35 = 0.73$ of the two-photon emission can ionize H I from $n = 2$. In principle, charge transfer between He II and C I may be important. Since the energy difference between the system before and after the collision is ~ 13.3 eV, the rate is likely to be very small for nonradiative charge transfer. Also radiative charge transfer is estimated to be slow. Although a high rate therefore seems implausible, we have estimated its effects, assuming a rate of $10^{-9}\ {\rm cm^{-3}\ s^{-1}}$. The result is that helium becomes nearly completely neutral, while the C II fraction increases to 60%–80%. Since the radiative recombination rate of C II is larger than for He II, the total electron fraction decreases from 1.74×10^{-2} without charge transfer to 1.11×10^{-2} at 500 days. The electrons come exclusively from C II. The optical depth of C I is, however, still very high. The He I emission above 11.26 eV is therefore still absorbed by C I, but the intensity of the two-photon emission is decreased to the level set by nonthermal excitation. Only a fraction $(11.26/24.5)\eta_{\rm ion}$ of the energy therefore emerges as C I recombination emission, of which only 60% is above 3.4 eV. The fate of the energy going into excitation of He I $2s\ ^1P$ remains unchanged. *If* charge transfer is important, the UV efficiency from the helium zone therefore decreases from 0.36 to 0.24 at 500 days. The remaining fraction of the He II ionization energy (corresponding to 13.3 eV of the 24.5 eV) goes into heating of the gas. We have also investigated the effects of Penning ionization of the $2s\ ^1S$ and $2s\ ^3S$ levels, using a typical cross section of $7 \times 10^{-16}\ {\rm cm^2}$ (Bell, Dalgarno, & Kingston 1968), and we found this process to be unimportant, due to the low population of the excited levels. In the following we neglect charge transfer between He II and C I.

As an example, we calculate $\epsilon_{\rm He}$ at $t = 500$ days, which corresponds to $x_e = 0.017$. For this x_e, $\sim 42\%$ of the deposited energy goes into ionization, and $\sim 15\%$ into excitation of He I. Therefore, the fraction of the energy absorbed in the helium zone which can ionize hydrogen from the $n = 2$ level is $\epsilon_{\rm He} \sim (0.63 \times 0.60 + 0.35) \times [0.42 \times (20.6/24.5) + 0.15] = 0.37$. In Figure 8 $\epsilon_{\rm He}$ is shown as a function of time, and thus for other values of x_e.

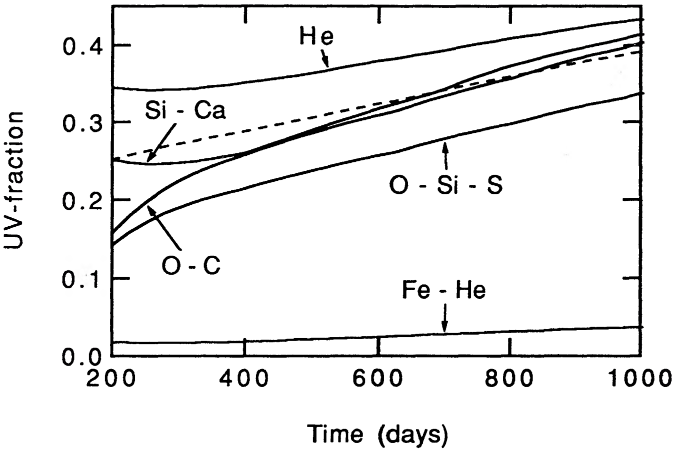

FIG. 8.—Fraction, ϵ_i, of the deposited energy emerging as UV radiation below 3646 Å for the different composition zones as a function of time. The dashed line is the averaged UV fraction in the case of a macroscopically mixed core, with composition from the 10H model by Woosley (1988).

In the helium-nitrogen zone, N I takes the role of C I for the absorption of the He I emission above 14.53 eV, while C I dominates between 11.23 and 14.53 eV. No calculations of the N I recombination cascade is available. The most important transitions have wavelengths between 1000 and 1500 Å, and we estimate the mean wavelength to ~ 1200 Å. The UV efficiency is thus $\sim (853/1200) = 0.71$. Thirty-nine percent of the He I two-photon emission can ionize N I. Adding the contribution from C I, and the two-photon emission between 3.4 and 11.26 eV as above, we find $\epsilon_{\rm He} \sim 0.39$ at $t = 500$ days. This is close to the value from the helium-carbon zone, and we therefore treat both regions together in terms of the UV emission.

The He I two-photon continuum may also ionize other ions with low ionization potentials, for example, Na I, Ca I, Mg I, and Si I. We find these elements to be almost completely ionized with $n_{\rm Na\,I}/n_{\rm Na\,II} \sim 1 \times 10^{-4}$, $n_{\rm Ca\,I}/n_{\rm Ca\,II} \sim 1 \times 10^{-4}$, $n_{\rm Mg\,I}/n_{\rm Mg\,II} \sim 4 \times 10^{-4}$, and $n_{\rm Si\,I}/n_{\rm Si\,II} \sim 6 \times 10^{-6}$ at $t = 500$ days.

In the oxygen zone the nonthermal excitations and recombinations result in O I 1302 and 1356 Å, which are both optically thick,

$$\tau(1302\ \text{Å}) \sim 2 \times 10^8 \left(\frac{M}{4\,M_\odot}\right)\left(\frac{V_{\rm core}}{2000\ {\rm km\ s^{-1}}}\right)^{-3}\left(\frac{t}{300\ {\rm d}}\right)^{-2} \tag{33}$$

and

$$\tau(1356\ \text{Å}) \sim 9 \times 10^2 \left(\frac{M}{4\,M_\odot}\right)\left(\frac{V_{\rm core}}{2000\ {\rm km\ s^{-1}}}\right)^{-3}\left(\frac{t}{300\ {\rm d}}\right)^{-2} . \tag{34}$$

At late epochs radiative de-excitation is likely to dominate over the collisional de-excitation for both lines. At ~ 300 days the ratio of collisional de-excitation to radiative de-excitation for the 1302 Å line is ~ 0.4, and for the 1356 Å line ~ 0.05, and these numbers decrease rapidly with time. A few percent of the deposited energy also goes into nonthermal excitation and ionization of carbon, silicon, and sulphur. Recombinations of these ions are discussed below. In the oxygen-silicon-sulphur region $\sim 5\%$ less energy emerges in the UV, compared to the oxygen-carbon zone (Fig. 8). This is a result of the large optical depth of the Si I continuum in the former region. Therefore, the O I lines are absorbed by Si I and 75% of the energy is emitted above 3.4 eV in the recombination of Si II (see below). In the oxygen-carbon region the silicon abundance is smaller, and the O I emission can escape freely.

Also the O I 1302 and 1356 Å lines can ionize the elements with low ionization potential (Fransson & Chevalier 1989). At $t = 500$ days $n_{\rm Ca\,I}/n_{\rm Ca\,II} \sim 2 \times 10^{-4}$, $n_{\rm Na\,I}/n_{\rm Na\,II} \sim 1 \times 10^{-4}$, $n_{\rm Mg\,I}/n_{\rm Mg\,II} \sim 8 \times 10^{-3}$, and $n_{\rm Si\,I}/n_{\rm Si\,II} \sim 5 \times 10^{-6}$. The continua of Ca I and Na I are optically thin in both regions.

In the silicon-calcium zone recombination and nonthermal excitation to the triplet and singlet levels in Si I and S I give rise to several strong lines in the UV. Unfortunately, recombination spectra of these elements are lacking. The Si I triplet levels result in UV transitions in the range 1900–2900 Å plus the $4s\ ^1P$–$3p^2\ ^1S$ transition at 3905 Å, while the singlet levels give rise to transitions in the range 1700–2500 Å. For S I, the triplet emission is in the range 1300–1800 Å, while that of the singlet lines is 1450–1800 Å. Each recombination to the singlets populates the metastable ^1S and ^1D levels. The ^1S level decays to the ^1D level by emiting a 1.0991 μm photon for Si I and a 7726 Å photon for S I. In the transition from the ^1D level to the ground state a 1.6455 or 1.6068 μm photon is emitted in Si I, and a 1.0820 or 1.1306 μm photon in S I. Recombination may therefore, in addition to collisional excitation, be important for the emission in these lines. In our calculations we assume that every recombination and nonthermal excitation of Si I and S I result in UV emission with an averaged wavelength of ~2000 Å for Si I, and ~1500 Å for S I. The ionization thresholds of Si I and S I correspond to 1520 and 1200 Å, respectively, and we therefore find that a fraction 1520 Å/2000 Å = 0.76 of the energy going into Si I and a fraction 1200 Å/1500 Å = 0.80 of the energy going into S I results in UV emission. The S I UV photons can ionize Ca I, Mg I, Na I, Fe I, Si I (photons with $\lambda \leq 1520$ Å), while the Si I UV photons can ionize Ca I and Na I. Of these elements calcium is the most abundant with a number fraction of 2.6% and we find that this element is almost completely ionized by the UV radiation with $n_{\rm Ca\,I}/n_{\rm Ca\,II} \sim 2 \times 10^{-3}$ at $t = 500$ days.

In the innermost core the dominant elements are iron and helium. Most of the excitations and ionizations of He I result in two-photon emission (see above). The probability for the 584 Å photons to be destroyed by continuum absorption by Fe I or Fe II is

$$P_{\rm cont} \sim [2 \times 10^{-4} X(\text{Fe I}) + 2 \times 10^{-6} X(\text{Fe II})] \times \left[\frac{X(\text{Fe})}{0.44}\right]\left(\frac{T}{5000\ \text{K}}\right)^{0.5}, \tag{35}$$

where X(Fe I) and X(Fe II) are the relative fractions of Fe I and Fe II, respectively. $P_{\rm cont}$ is much less than $P_{\rm branch}$, and as in the helium zone, most of the nonthermal energy going into helium is therefore emitted in the 2.08 μm line plus two-photon continuum. Of the latter, 84% of the energy results in photons with $h\nu \gtrsim 7.90$ eV, which can ionize Fe I, while 25% of the energy can ionize Fe II with an ionization potential of 16.2 eV. For the same reason as for C I and He II in the helium zone, we do not expect charge transfer between He II and Fe I or Fe II to be important. The effect of charge transfer would be to decrease ϵ in the same way as discussed for the helium zone.

The Fe I and Fe II spectra are similar in nature. The ground state is split into five fine-structure levels, with a separation of ~0.05 eV, giving rise to far-IR lines at 24.0, 34.7, and 54.3 μm for Fe I and at 26.0, 35.3, 51.3, and 87.4 μm for Fe II. Between 1 and 2 eV above the ground state there are a number of metastable levels, connected to the ground state by forbidden lines in the optical and near-IR regions of the spectrum. Finally, there are a large number of resonance levels with excitation energies above ~3.2 eV for Fe I, and above ~4.8 eV for Fe II. These are connected to the ground state by transitions in the UV, and to the intermediate, metastable levels by optical transitions. The optical depths of the resonance lines are of the order

$$\tau \sim 2 \times 10^{8}\left[\frac{X(\text{Fe})}{0.44}\right]\left(\frac{M}{4\,M_\odot}\right)\left(\frac{\lambda}{2500\ \text{Å}}\right)^{3} \times \left(\frac{A_{21}}{10^{8}\ \text{s}^{-1}}\right)\left(\frac{V_{\rm core}}{2000\ \text{km s}^{-1}}\right)^{-3}\left(\frac{t}{300\ \text{d}}\right)^{-2}. \tag{36}$$

Since the branching ratios to the metastable levels are $\sim 10^{-3}$, most of the flux escapes as optical radiation.

In Figure 8 we show the resulting γ-ray to UV conversion factors for the different zones, assuming a uniformly, macroscopically mixed γ-ray source. In the calculations we have for each epoch and for each zone estimated the electron fraction from Figure 7, and then calculated the deposition and UV conversion for this value of x_e. To get the total nonthermal to UV efficiency, the separate values of ϵ_i should be weighted by the energy input into each zone. For a macroscopically mixed case

$$\epsilon = \frac{\sum_i M_i \epsilon_i}{M_{\rm core}}, \tag{37}$$

where M_i is the mass of zone i. In an unmixed case

$$\epsilon = \frac{\sum_i e^{-\tau_{\gamma,i}}(1 - e^{-\Delta\tau_{\gamma,i}})\epsilon_i}{\sum_i e^{-\tau_{\gamma,i}}(1 - e^{-\Delta\tau_{\gamma,i}})}. \tag{38}$$

The dashed line in Figure 8 shows the averaged ϵ for the mixed case, and with the M_i in equation (37) taken from the 10H composition.

The increase of ϵ_i with time for all zones is a result of the decrease of x_e with time. A larger fraction of the deposited nonthermal energy then goes into excitation and ionization, and therefore into recombination emission in UV lines. That the UV efficiency is largest for the helium zone is consistent with the fact that x_e is smallest in this zone (Fig. 7), as well as a somewhat higher fraction of UV photons in the recombination cascade. The low UV efficiency of the iron-core is mainly due to the high optical depth of the Fe lines, which converts most of the UV emission into optical emission.

In our calculations of ϵ, we have neglected contributions due to thermal, collisional excitation. The most important case is Mg II λ2800, where most of the emission is coming from the oxygen-silicon-sulphur and helium zones. For expansion velocities typical of Type II supernovae (less than ~2500 km s^{-1}) Fransson & Chevalier (1989) find that less than ~5% of the core emission emerges in this line. For higher velocities, and thus lower densities, this fraction may increase to ~10%. The neglect of this line should therefore only introduce a minor underestimate of the UV flux. In addition to these contributions from the core to the UV intensity, there is a source of UV emission from the Lyα and two-photon continuum of hydrogen in the envelope (see next section).

4.3. *Ionization of Hydrogen and the Hα Emission in Type II Supernovae*

The ionization equilibrium in the hydrogen envelope of SN 1987A has recently been discussed by, for example, Chugai

(1987), Xu & McCray (1991a), Xu et al. (1992), and Fransson (1991). They find that the observed ionization of hydrogen can not be explained by either thermal or nonthermal ionization from the ground state, due to the high ionization potential of 13.6 eV. This is directly connected with the problem of explaining the Hα line, mainly arising as a result of recombination. The most likely explanation of this problem is ionization from the excited $n = 2$ level in H I, as first suggested by Kirshner & Kwan (1975). Ionization from $n = 2$ costs a factor of 4 less energy than ionization from the ground state. Trapping of Lyα results in a significant population of the $n = 2$ level, leading to a nonnegligible opacity in the Balmer continuum, and making ionization from $n = 2$ efficient. UV lines below 3646 Å from the core and the helium zone, as well as, for example, Lyα and H I two-photon emission from the hydrogen envelope, can then ionize the excited hydrogen atoms. This is the main motivation for calculating the fraction of the energy emerging as UV lines from the different zones as a function of time, shown in Figure 8.

From the statistical equations for the $n = 2$ level and the continuum one can solve for the populations of the first two levels, as well as for x_e (e.g., Fransson 1991). From the $n = 2$ population one can then calculate the Balmer optical depth of the hydrogen envelope, with the result

$$\tau_B(\nu) = \sigma_B(\nu)\int n_2\,dr = \sigma_B(\nu)\int n_1 \frac{\Gamma_2 + \Gamma_c + P_1}{A_{2\gamma} + A_{L\alpha}\beta_{L\alpha}}\,dr\,. \qquad (39)$$

Here $\sigma_B(\nu) \approx 1.5 \times 10^{-17}(\nu/\nu_0)^{-2.9}$ cm^{-2} is the photoionization cross section from the $n = 2$ level, n_1 and n_2 the populations of the $n = 1$ and 2 levels, and Γ_2 and Γ_c the nonthermal excitation rates to $n = 2$ and the continuum, respectively. Also, Γ_c is determined from equations (13) and (22), P_1 is the photoionization rate from the $n = 1$ level, $A_{2\gamma}$ and $A_{L\alpha}$ the transition probabilities for the two-photon and the Lyα transition, respectively, and $\beta_{L\alpha} = (1 - e^{-\tau_{L\alpha}})/\tau_{L\alpha} \approx 1/\tau_{L\alpha}$, the escape probability for the Lyα line. We neglect thermal collision terms, which in most cases is a good approximation.

For large metal abundances charge transfer between metals and hydrogen can be an important process and has been discussed by Xu & McCray (1991a). They find that in the case of total mixing of hydrogen and metals, charge transfer can significantly reduce the ionization of hydrogen. For this to be the case the mixing must be microscopic. As we have already argued, this is however, not likely to be the case. For ordinary solar abundances the ionization of hydrogen is not seriously affected by charge transfer, although ions like O I and O II may be affected. Therefore, our neglect of charge transfer should be justified.

As is evident from, for example, equation (39), the density in the hydrogen-rich gas is crucial for the emission. The one-dimensional hydrodynamical model of SN 1987A by Shigeyama et al. (1988) has a density, which can be approximated by

$$n_H(r, t) = 6.7 \times 10^8\left(\frac{R_{\rm core}}{r}\right)t_{\rm yr}^{-3}\ {\rm cm}^{-3} \qquad (40)$$

outside of $R_{\rm core}$, corresponding to $\sim$2000 km s^{-1}. Two-dimensional models show that the hydrogen-rich gas can penetrate deep into the core region (e.g., Fryxell et al. 1991; Herant & Benz 1991). This is also indicated by the observations, which show a maximum hydrogen expansion velocity not much higher than that of the metal-rich gas, $\sim$2000 km s^{-1} at late epochs (e.g., Phillips & Williams 1991). From the simulations by Fryxell et al. we find that a mass $M({\rm H})_{\rm core} \sim 1.0\ M_\odot$ of hydrogen is mixed into the core with a velocity of less than 2000 km s^{-1}. We estimate the filling factor of the hydrogen-rich gas in the core to $f_H \approx 0.4$, resulting in a density for this component of

$$n_H(r, t) = 2.2 \times 10^9\left(\frac{f_H}{0.4}\right)^{-1}\left[\frac{M({\rm H})_{\rm core}}{1\ M_\odot}\right] \times \left(\frac{V_{\rm core}}{2000\ {\rm km\ s^{-1}}}\right)^{-3} t_{\rm yr}^{-3}\ {\rm cm}^{-3}\,. \qquad (41)$$

It should be emphasized that this density is quite uncertain, and we therefore treat $M({\rm H})_{\rm core}$ and f_H as scaling parameters. Outside of the core, equation (40) is likely to give a reasonable estimate of the density. Because of the decrease of the density with radius and the concentration of the ^{56}Ni to the core region, only a minor fraction of the hydrogen emission is, however, likely to come from gas outside of the core, as indicated by the line widths in the late spectra (see below).

For the energy input to the various components we also need the γ-ray optical depth of the hydrogen-rich gas in the core, $\tau_{\gamma,{\rm H}}$, and the heavy element–rich gas, $\tau_{\gamma,{\rm core}}$. If the two components are well mixed, macroscopically, $\tau_{\gamma,{\rm core}}$ is given by equation (19), and

$$\tau_{\gamma,{\rm H}} = 0.06 m_p f_H n_H R_{\rm core} = 0.56\left[\frac{M({\rm H})_{\rm core}}{1\ M_\odot}\right]\left(\frac{V_{\rm core}}{2000\ {\rm km\ s^{-1}}}\right)^{-2} t_{\rm yr}^{-2}\,. \qquad (42)$$

The total column density implied by equations (28) and (41) extrapolated back to 3.6*h*, 3.5×10^8 g cm^{-2}, agrees well with that obtained by Fryxell et al. (1991), $\sim 2.7(\pm 1.0) \times 10^8$ g cm^{-2}. Of this $\sim$20% is due to the hydrogen-rich gas. Outside of the core, from $V_{\rm core}$ $\sim$2000 km s^{-1} to the maximum envelope velocity of $\sim$5000 km s^{-1}, we estimate from equation (40) that an additional

$$\tau_{\gamma,{\rm env}} = 0.39 t_{\rm yr}^{-2} \qquad (43)$$

contributes to the total γ-ray depth of the hydrogen-rich gas.

With the density from equation (41), $\beta_{L\alpha}A_{L\alpha} \approx A_{L\alpha}/\tau_{L\alpha} = 4.7 \times 10^{15}/n_1 t \sim 6.8 \times 10^{-2}\ t_{\rm yr}^2$ s^{-1}. Assuming equipartition of 2*s* and 2*p*, $A_{2\gamma} = 8.3/4 = 2.1$, and we find that $A_{L\alpha}\beta_{L\alpha} \ll A_{2\gamma}$ for the first 5 years. This means that two-photon emission will be more important than Lyα in the de-excitation of $n = 2$. Since $P_1 \ll \Gamma_c$ we obtain

$$\tau_B(\nu) \approx \frac{\sigma_B(\nu)}{A_{2\gamma}}\int_0^{R_{\rm core}} n_1(\Gamma_c + \Gamma_2)dr\,. \qquad (44)$$

The rate of ionizations from the ground state is given by

$$\Gamma_c = 4.0 \times 10^{-6} D_\gamma\left(\frac{V_{\rm core}}{2000\ {\rm km\ s^{-1}}}\right)^{-2}\left(\frac{M_{\rm Ni}}{0.1\ M_\odot}\right) \times \left(\frac{\chi_{\rm eff}}{40\ {\rm eV}}\right)^{-1}\frac{e^{-t/111\,{\rm d}}}{t_{\rm yr}^2}\ {\rm s}^{-1}\,. \qquad (45)$$

From Tables 2A and 3 we estimate that $\Gamma_2 \approx 0.9\Gamma_c$. Inserting numerical values for τ_B, and integrating D_γ over the core we find

$$\tau_B(\lambda) \approx \frac{2.1 \times 10^3}{(1 + \tau_{\gamma,{\rm core}})}\left(\frac{\lambda}{3464\ {\rm Å}}\right)^{2.9}\left(\frac{f_H}{0.4}\right)^{-1}\left[\frac{M({\rm H})_{\rm core}}{1\ M_\odot}\right] \times \left(\frac{V_{\rm core}}{2000\ {\rm km\ s^{-1}}}\right)^{-4}\left(\frac{M_{\rm Ni}}{0.1\ M_\odot}\right)\left(\frac{\chi_{\rm eff}}{40\ {\rm eV}}\right)^{-1}\frac{e^{-t/111\,{\rm d}}}{t_{\rm yr}^4}\,. \qquad (46)$$

The factor $(1 + \tau_{\gamma,\mathrm{core}})^{-1}$ comes from an approximate interpolation between the optically thin and thick γ-ray deposition. From this expression we see that the optical depth is larger than one at least up to ~ 600 days, after which it decreases exponentially. An important factor, not included, is that resonance scattering in the UV can increase the optical depth substantially. The effective absorption of the UV photons is then increased by a factor $\sim V_{\mathrm{core}}/\Delta V_{\mathrm{res}}$, where ΔV_{res} is the typical velocity separation of the UV resonance lines. This factor can be large and will be subject to a separate study.

In the same way as for the He II $\lambda 584$ line, Balmer continuum absorption could be important for the Lyα line. This would decrease the $n = 2$ population, and a self-consistent calculation of the Balmer optical depth would be necessary. In analogy with equation (32) we have therefore calculated the continuum destruction probability

$$P_{\mathrm{cont}} \sim 1.3 \times 10^{-10}\left(\frac{T}{5000\ \mathrm{K}}\right)^{0.5}\left(\frac{V_{\mathrm{core}}}{2000\ \mathrm{km\ s^{-1}}}\right)^{-2} \times \left(\frac{M_{\mathrm{Ni}}}{0.1\ M_{\odot}}\right)\left(\frac{\chi_{\mathrm{eff}}}{40\ \mathrm{eV}}\right)^{-1} \frac{e^{-t/111\,\mathrm{d}}}{t_{\mathrm{yr}}^{2}}\,, \tag{47}$$

which should be compared to the branching probability of the two-photon decay, $P_{\mathrm{branch}} = 4.5 \times 10^{-9}$. Continuum absorption of Lyα is therefore unimportant, and our calculation of τ_{B} is consistent.

As long as the Balmer continuum is optically thick, the UV intensity is given by $J_\nu \approx S_\nu = j_\nu/\kappa_\nu = \epsilon_\nu J_\gamma \sigma_\gamma n/\kappa_\nu$, where ϵ_ν is the efficiency of converting the nonthermal energy input to emission in the interval ν to $\nu + d\nu$,

$$\epsilon = \int_{3.4\,\mathrm{eV}}^{\infty} \epsilon_\nu\, d\nu\,.$$

Therefore, since $\kappa_\nu \approx \sigma_{\mathrm{B}}(\nu) n_2$,

$$P_2 = 4\pi \int_{\nu 0} \frac{J_\nu \sigma_{\mathrm{B}}(\nu) d\nu}{h\nu} = \frac{4\pi J_\gamma \sigma_\gamma n}{n_2} \int_{\nu 0} \frac{\epsilon_\nu\, d\nu}{h\nu} \approx \epsilon A_{2\gamma} \frac{\chi_{\mathrm{eff}}}{\langle h\nu \rangle}\,, \tag{48}$$

where $\langle h\nu \rangle$ is the average energy of the ionizing radiation in the Balmer continuum. This shows explicitly the importance of determining the UV efficiency ϵ. In § 4.2 we found that $\epsilon \approx 0.3$, and since $\chi_{\mathrm{eff}}/\langle h\nu \rangle \approx 10$, we find that $P_2 \approx 3A_{2\gamma}$.

If we for simplicity neglect $A_{2\gamma}$ compared to P_2, one finds that the electron density is determined by

$$n_+ n_e = \frac{P_2(\Gamma_2 + \Gamma_c + P_1)}{(A_{2\gamma} + A_{\mathrm{L}\alpha} \beta_{\mathrm{L}\alpha})\alpha_C} n_1\,. \tag{49}$$

Here α_C is the total recombination rate in case C (e.g., Xu & McCray 1991) and is given by

$$\alpha_C = \sum_{k=3}^{\infty} \alpha_k\,,$$

if the Balmer continuum is thick. In general, one can interpolate between the case C and case B rates by using $\alpha_C = \alpha_{\mathrm{B}} - (1 - \beta_{\mathrm{B}})\alpha_2$, where β_{B} is the average escape probability in the Balmer continuum. Similar more accurate expressions have been derived by Xu et al. (1992) and Fransson (1991). As a rough approximation we take $\beta_{\mathrm{B}} \approx e^{-\tau_{\mathrm{B}}}$. Since $\Gamma_c \gg P_1$ and $A_{2\gamma} \gg \beta_{\mathrm{L}\alpha} A_{\mathrm{L}\alpha}$, one finds

$$n_+ n_e \approx n_e^2 = \frac{P_2(\Gamma_c + \Gamma_2)}{A_{2\gamma}\alpha_C} n_1\,. \tag{50}$$

Inserting equations (13) and (48), we get

$$n_e^2 \approx \frac{1.9\epsilon D_\gamma \sigma_\gamma L_\gamma}{4\pi \langle h\nu \rangle \alpha_C R_{\mathrm{core}}^2} n_1\,. \tag{51}$$

Using our in § 4.2 derived value of $\epsilon \approx 0.3$, $D_\gamma \approx 2$, and $\langle h\nu \rangle \approx 5$ eV, we get

$$n_e \approx 1.0 \times 10^4 \left(\frac{T}{5000\ \mathrm{K}}\right)^{0.44}\left(\frac{V_{\mathrm{core}}}{2000\ \mathrm{km\ s^{-1}}}\right)^{-1}\left(\frac{M_{\mathrm{Ni}}}{0.1\ M_{\odot}}\right)^{1/2} \times \frac{e^{-t/222\,\mathrm{d}}}{t_{\mathrm{yr}}} n^{1/2}\ \mathrm{cm}^{-3}\,. \tag{52}$$

Assuming that the hydrogen density is given by equation (41) we obtain

$$x_e \approx 0.22\left(\frac{f_{\mathrm{H}}}{0.4}\right)^{1/2}\left[\frac{M(\mathrm{H})_{\mathrm{core}}}{1\ M_{\odot}}\right]^{-1/2}\left(\frac{T}{5000\ \mathrm{K}}\right)^{0.44} \times \left(\frac{V_{\mathrm{core}}}{2000\ \mathrm{km\ s^{-1}}}\right)^{1/2}\left(\frac{M_{\mathrm{Ni}}}{0.1\ M_{\odot}}\right)^{1/2} t_{\mathrm{yr}}^{1/2} e^{-t/222\,\mathrm{d}}\,, \tag{53}$$

which is valid for $\tau_{\mathrm{B}} > 1$. This gives a fairly slow decrease of x_e up to ~ 500 days.

The electron density has been estimated observationally by Moseley et al. (1989) and Aitken et al. (1988) from the infrared continuum, assuming this to be due to free-free emission, as well as from the H I recombination lines in the IR. Repeating their analysis, and assuming that all free-free emission comes from hydrogen, we find from the IR continuum at 10 μm,

$$x_e = 3.6 \times 10^{-2} S_{10\,\mu\mathrm{m}}^{1/2}\left(\frac{f_{\mathrm{H}}}{0.4}\right)^{1/2}\left[\frac{M(\mathrm{H})_{\mathrm{core}}}{1\ M_{\odot}}\right]^{-1} \times \left(\frac{V_{\mathrm{core}}}{2000\ \mathrm{km\ s^{-1}}}\right)^{3/2}\left(\frac{T_e}{5000\ \mathrm{K}}\right)^{1/4} e^{719\ \mathrm{K}/T_e t_{\mathrm{yr}}^{3/2}}\,, \tag{54}$$

where $S_{10\,\mu\mathrm{m}}$ is the 10 μm continuum flux in Jy. On days 257 and 370 Aitken et al. find $S_{10\,\mu\mathrm{m}} = 14$ and 5.4, corresponding to $x_e = 0.093$ and 0.099, respectively. The free-free component may also have a contribution from the metal- and helium-rich gas. Using our calculated values of x_e in these zones, masses of the components from the 10H model, and a core density given by equation (28), we have calculated the free-free flux from the various zones relative to that of hydrogen. Because of the larger masses involved, the helium- and oxygen-rich zones dominate. We find that on day 257 the helium zone has a total free-free flux equal to 3.7% of hydrogen, while the oxygen zone has 3.4%. On day 370 the corresponding numbers are 5.7% and 5.5%, respectively. The total nonhydrogenic contribution is 7.9% and 12.6% on these days. From these estimates it is likely that most of the free-free emission originates in the hydrogen-rich gas.

The H I recombination lines are somewhat less model dependent for estimating x_e. For the H I 7–6 line we obtain from Aitken et al.'s (1988) observation on day 257

$$x_e = 0.057\left(\frac{f_{\mathrm{H}}}{0.4}\right)^{1/2}\left[\frac{M(\mathrm{H})_{\mathrm{core}}}{1\ M_{\odot}}\right]^{-1}\left(\frac{T_e}{5000\ \mathrm{K}}\right)^{0.42} \times \left(\frac{V_{\mathrm{core}}}{2000\ \mathrm{km\ s^{-1}}}\right)^{3/2}\,. \tag{55}$$

On day 370 the coefficient is 0.073, which shows that the degree of ionization is nearly constant over this period, despite a factor of 3 decrease in both density and γ-ray luminosity.

These observationally determined values of x_e should be compared with equation (53). Setting all parameters in brackets equal to unity we obtain $x_e = 0.058$ on day 257, and $x_e = 0.041$ on day 370. The agreement between observations and theory is therefore fairly satisfactory. The discrepancy between observations and theory is likely to be caused by our rough estimates of $f_{\rm H}$ and $M({\rm H})_{\rm core}$, as well as the neglect of emission from the region outside of the core. Another important result is the slow decrease with time implied by equation (53), which is in good agreement with the nearly constant level of ionization found by Aitken et al. (1988) during the observed period. Xu et al. (1992) estimate the electron fraction in a similar way and find that agreement with their model and observations requires a source of UV photons closely corresponding to the value of ϵ estimated in this paper.

Having an estimate of the Balmer optical depth with time, we can now calculate the total energy emitted in the Hα line from the core and the envelope. The fraction of the γ-ray energy absorbed in the helium and oxygen core is $(1 - e^{-\tau_{\gamma,\rm core}})L_\gamma$, of which a fraction ϵ results in emission with $E > 3.4$ eV. The fraction which is absorbed by the Balmer continuum is $(1 - e^{-\tau_{\rm B}})\epsilon$. Here $\tau_{\rm B}$ should be considered as an average optical depth at the wavelength where most of the UV emission is emitted. The $\alpha_{\rm 3eff}$ is the effective recombination coefficient to the $n = 3$ level, including both direct recombination and recombinations to higher levels, followed by cascading down to the $n = 3$ level. Thus, $\alpha_{\rm 3eff}/\alpha_C$ is the fraction of the recombinations giving rise to an Hα photon. In terms of energy, a fraction $h\nu/\chi_2 = 5/9$ emerges in the Hα line. The luminosity in the Hα line due to $n = 2$ ionizations from the core is therefore

$$L({\rm H}\alpha) \approx \frac{5}{9}\,\epsilon(1 - e^{-\tau_{\rm B}})(1 - e^{-\tau_{\gamma,\rm core}})\,\frac{\alpha_{\rm 3eff}}{\alpha_C}\,L_\gamma\,. \qquad (56)$$

In addition, there is also a contribution from direct excitation and ionization in the hydrogen-rich gas. The ionization rate per volume is $n_1\Gamma_c$, and the fraction of L_γ emerging as recombination radiation in Hα is $(5/36)(13.6/\chi_{\rm eff})(1 - e^{-\tau_{\gamma,\rm H}})(\alpha_{\rm 3eff}/\alpha_C)L_\gamma$. Here $\tau_{\gamma,\rm H}$ is the γ-ray optical depth of the hydrogen-rich material in the core, given by equation (42). Most of the de-excitations from $n = 2$ occur by two-photon emission, since $A_{2\gamma} \gg \beta_{{\rm L}\alpha} A_{{\rm L}\alpha}$. A fraction 0.88 of this emission adds to the UV flux above 3.4 eV from the core and gives in the same way an Hα contribution $(3/4) \times 0.88 \times (5/9)\,(13.6/\chi_{\rm eff})(1 - e^{-\tau_{\rm B}})(1 - e^{-\tau_{\gamma,\rm H}})(\alpha_{\rm 3eff}/\alpha_C)L_\gamma$. Direct excitations to $n = 2$ result in two-photon emission, and therefore add an additional factor $[1 + (\Gamma_2/\Gamma_c)] \sim 1.9$ to the Hα emission. The total Hα luminosity is then

$$L({\rm H}\alpha) = \left\{\frac{5}{9}\,(1 - e^{-\tau_{\rm B}})\left[\epsilon(1 - e^{-\tau_{\gamma,\rm core}}) + 1.25\,\frac{13.6}{\chi_{\rm eff}}\,(1 - e^{-\tau_{\gamma,\rm H}})\right] + \frac{5}{36}\,\frac{13.6}{\chi_{\rm eff}}\,(1 - e^{-\tau_{\gamma,\rm H}})\right\}\frac{\alpha_{\rm 3eff}}{\alpha_C}\,L_\gamma\,. \qquad (57)$$

If $\tau_{\rm B} > 1$, $\alpha_{\rm 3eff} \approx \alpha_C$, so

$$L({\rm H}\alpha) = \frac{5}{9}\left[\epsilon(1 - e^{-\tau_{\gamma,\rm core}}) + 1.50\,\frac{13.6}{\chi_{\rm eff}}\,(1 - e^{-\tau_{\gamma,\rm H}})\right]L_\gamma\,, \qquad (58)$$

while if $\tau_{\rm B} \ll 1$

$$L({\rm H}\alpha) = \frac{5}{36}\,\frac{13.6}{\chi_{\rm eff}}\,(1 - e^{-\tau_{\gamma,\rm H}})\,\frac{\alpha_{\rm 3eff}}{\alpha_{\rm B}}\,L_\gamma\,. \qquad (59)$$

The value of ϵ from the core is given in Figure 8, and for $\tau_{\gamma,\rm core}$ and $\tau_{\gamma,\rm H}$ we use equations (19) and (42); $\tau_{\rm B}$ is calculated from a full solution of the equilibrium equations, including collisional effects, and $\chi_{\rm eff}$ is obtained from Table 2, with x_e evaluated from equation (53).

A factor not included in the calculation of ϵ is that the scattering by the UV resonance lines, and the concomitant redshifting of the photons, may decrease the energy of the UV radiation reaching the hydrogen envelope substantially. Because of the increasing energy gaps between the resonance lines above $\sim$3000 Å, we do not, however, expect this to shift a substantial part of the energy longward of the Balmer limit. On the other hand, as we have already pointed out, resonance scattering will increase the effective value of $\tau_{\rm B}$ above that given by equation (46). These effects will be discussed in a separate paper.

Especially at early times collisional effects can be important. In particular, collisional de-excitation of the $n = 2$ and 3 levels decreases the Balmer depth compared to that given by equation (46), as well as the efficiency of the Hα emission compared to pure recombination. This effect is included in our calculations. Collisional excitation of Hα can increase the strength of this line for temperatures above 5000 K earlier than 300–400 days. Since this process is sensitive to the assumed temperature, we defer the calculation of this effect to a later paper, where the full thermal balance is calculated.

Outside of the core, the Balmer continuum is transparent after a year, and only nonthermal ionizations from the ground state contribute to the Hα luminosity. The luminosity of this component is thus given by equation (59) with $\tau_{\gamma,\rm H}$ replaced by $\tau_{\gamma,\rm env}$ from equation (43). The Hα line is therefore expected to have a high-velocity wing with total luminosity of

$$L({\rm H}\alpha)_{\rm wing} = 2.3 \times 10^{-2}\left(\frac{\chi_{\rm eff}}{40\ {\rm eV}}\right)^{-1}\tau_{\gamma,\rm env}L_\gamma\,, \qquad (60)$$

since $\tau_{\gamma,\rm env} < 1$, after $\sim$230 days. Therefore, only $\sim$2.3% of the absorbed γ-ray energy in the envelope emerges as Hα emission. For an arbitrary power-law density in the envelope, given by $n_{\rm H} = n_{\rm core}(R_{\rm core}/r)^\gamma$, the line luminosity from the envelope region as a function of the dimensionless frequency x, is given by

$$\frac{dL(x)}{dx} = L_0\left[1 - \left(\frac{V_{\rm core}}{V_{\rm env}}\right)^\gamma\right] \quad 0 < |x| < 1\,,$$
$$\frac{dL(x)}{dx} = L_0\left[\left(\frac{1}{x}\right)^\gamma - \left(\frac{V_{\rm core}}{V_{\rm env}}\right)^\gamma\right] \quad 1 < |x| < \frac{V_{\rm env}}{V_{\rm core}}\,, \qquad (61)$$

where

$$L_0 = \frac{1}{2}\,\frac{\alpha_{\rm 3eff}}{\alpha_{\rm B}}\,\frac{L_\gamma\sigma_\gamma}{\chi_{\rm eff}}\,\frac{n_{\rm core}}{\gamma}\,h\nu_{{\rm H}\alpha}R_{\rm core} = \frac{1}{2}\,L({\rm H}\alpha)_{\rm wing} \qquad (62)$$

and

$$x = \frac{\nu - \nu_0}{\nu_0}\,\frac{c}{V_{\rm core}}\,.$$

Therefore, by observing the wing of the Hα line with a high signal-to-noise ratio at late epochs, when the optical depth in

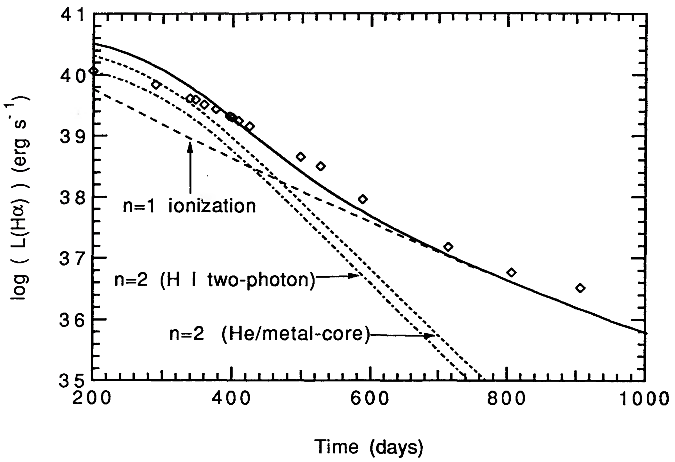

FIG. 9.—Comparison of the Hα luminosity from model calculations and observations (*diamonds*) of SN 1987A by Phillips & Williams (1991). The solid line gives the total Hα luminosity, while the dashed lines give the individual contributions from direct ionization of H I from $n = 1$, ionization from $n = 2$ by the H I two-photon emission, and ionization from $n = 2$ by the UV radiation from the helium-metal core.

the line is small, the density profile of the envelope can be determined.

In Figure 9 we compare the evolution of the Hα luminosity obtained from our model with observations of SN 1987A from Phillips & Williams (1991). In agreement with the bolometric light curve of Phillips & Williams, we take a ^{56}Ni mass of 0.071 $M_{\odot}$. In addition, we include ^{57}Ni with ^{57}Ni/^{56}Ni equal to 1.5 times the solar ^{57}Fe/^{56}Fe ratio (Danziger et al. 1991). In the figure we show the individual contributions to the luminosity from the γ-ray absorption in the hydrogen-rich gas, and the UV ionization by the two-photon emission and radiation from the helium-metal core. In general, there is very good agreement with the observations, given the simplicity of the model. Before ~300 days we overestimate the luminosity by a factor up to 2, at 200 days. The reason for this is presumably that the metal core is still optically thick in the UV continuum, and even in the optical region. Therefore, continuum destruction of especially the UV line emission is important, leading to a lower Hα flux. In addition, at these early times collisional excitation of Hα may be important. Between ~450 and ~600 days our values are somewhat lower than the observations. The reason for this may be that we have neglected the UV resonance scattering effect on the determination of τ_B. Inclusion of this will prolong the time when $\tau_B > 1$, and therefore also the epoch when UV excitation of $n = 2$ is important. In a future paper we hope to discuss this in more detail. After ~500 days direct ionization of hydrogen from $n = 1$, followed by recombination dominates the excitation. The last observation at 907 days clearly falls above the theoretical curve. This is further strengthened by the recent observations by Danziger et al. (1991) at ~1300 days, which show an Hα luminosity a factor of ~4 larger than our calculations. Other radioactive isotopes like ^{44}Ti are unlikely to contribute to the emission appreciably before ~1200 days. This also applies for the positrons from the ^{56}Co decay, which are only important after ~1400 days. Therefore, this indicates that an additional energy source may be needed after ~800 days.

5. CONCLUSIONS

We have calculated the γ-ray deposition for the different composition zones in core collapse supernovae. These results provide the starting point for the calculation of the ionization and temperature in the ejecta, as well as the spectrum. We find that the γ-ray excitation and ionization of individual elements are sensitive to the chemical composition and should be calculated for the specific case present. The results in Table 2 should be applicable for the most interesting cases. For Type Ia supernovae the results in § 3.2, the energy deposition in iron are of special interest. In a more general context, the nonthermal deposition for a gas of solar composition in Table 2A can be applied to, for example, AGNs.

As an important application we have used these results for calculating the ionization structure of the supernova ejecta and the formation of the Hα line. We find that the conversion of the emission from the recombination and nonthermal excitation involves a complicated series of degradation steps before escape. Of the total γ-ray energy absorbed a fraction ϵ, shown in Figure 8, gives rise to UV emission capable of ionizing hydrogen in the hydrogen-rich gas from the $n = 2$ level. From analytical arguments we calculate the efficiency of γ-ray to Hα conversion in SN 1987A and find good agreement with observations, except at late stages when an additional energy source may be required. The next step is a more detailed modeling of the ionization and scattering in the core and envelope, in particular the effects of the resonance scattering on the emergent spectrum and thermal effects on the state of ionization and emission. This will be addressed in a future paper. We finally add that the numerical fits to the nonthermal excitations in Table 2 can be obtained in digital form from the authors.

We are grateful to Anders Bárány, Peter Lundqvist, and Göran Scharmer for discussions, and to Dick McCray for several useful comments. This work is supported by the Swedish Natural Science Research Council (NFR).

APPENDIX

ATOMIC DATA

To calculate the energy deposition into the different channels one needs accurate cross sections both for excitation and ionization. The following ions are included in the calculations: H I, He I, He II, C I, C II, N I, N II, O I, O II, Ne I, Na I, Na II, Mg I, Mg II, Si I, Si II, S I, S II, Ar I, Ca I, Ca II, Fe I, Fe II, and Ni I.

Expressions for ionization cross sections are all taken from Arnaud & Rothenflug (1985), except for O I. O I ionizations to O II $^4S^o$, $^2D^o$, $^2P^o$, and $2s\,2p^4\,{}^4P$ are included separately, with cross sections from Laher & Gilmore (1990). Ionizations from the K-shell are unimportant for all metals, since the cross section at the K-threshold is down by a factor of at least the ratio of the outer shell ionization potential to the K-shell ionization potential, for example, for Fe I by a factor of ~10^{-3}.

TABLE 6

COLLISIONAL EXCITATION CROSS SECTIONS

Ion	Levels Included	References for Cross Sections	Levels for Which the Bethe Approximation Is Used
H I	$2s$, $2p$, $3s$, $3p$, $3d$, $4s$, $4p$, $4d$, $4f$	1, 2, 3, 4, 5, 6	…
He I	$2s\,^{1}S$, $2p\,^{1}P^{o}$, $3s\,^{1}S$, $3p\,^{1}P^{o}$, $3d\,^{1}D$,	…	…
	$2s\,^{3}S$, $2p\,^{3}P^{o}$, $3s\,^{3}S$, $3p\,^{3}P^{o}$, $3d\,^{3}D$	4, 7, 8, 9, 10, 11, 12	…
C I	$2p\,^{1}D$, $2p\,^{1}S$, $3s$, $3p$, $3d$, $4s$, $4p$, $4d$,	…	…
	$5s$, $5d$	13, 14, 15, 16	…
N I	$3s\,^{4}P$, $2s\,2p^{4}\,^{4}P$	…	$3s\,^{4}P$, $2s\,2p^{4}\,^{4}P$
O I	$2p\,^{1}D$, $2p\,^{1}S$, $3s\,^{3}S^{o}$, $3p\,^{3}P$, $3d\,^{3}D^{o}$, $4s\,^{3}S^{o}$,	…	…
	$4p\,^{3}P$, $4d\,^{3}D^{o}$, $3s\,^{5}S^{o}$, $3p\,^{5}P^{o}$, $3d\,^{5}D^{o}$,	…	…
	$4s\,^{5}S^{o}$, $4p\,^{5}P^{o}$, $4d\,^{5}D^{o}$, $3s'\,^{3}D^{o}$	17, 18	…
O II	$2s\,2p^{4}\,^{4}P$, $3s\,^{4}P$, $3d\,^{4}P$	…	$2s\,2p^{4}\,^{4}P$, $3s\,^{4}P$, $3d\,^{4}P$
Ne I	$3s\,^{3}P^{o}$, $3s\,^{1}P^{o}$	…	$3s\,^{3}P^{o}$, $3s\,^{1}P^{o}$
Na I	$3p\,^{2}P^{o}$, $3d\,^{2}D$, $4s\,^{2}S$, $4p\,^{2}P^{o}$, $4d\,^{2}D$,	…	…
	$5p\,^{2}P^{o}$, $6p\,^{2}P^{o}$, $7p\,^{2}P^{o}$	19, 20	…
Mg I	$3p\,^{1}P^{o}$, $4p\,^{1}P^{o}$, $5p\,^{1}P^{o}$	21	$4p\,^{1}P^{o}$, $5p\,^{1}P^{o}$
Mg II	$3p\,^{2}P^{o}$, $3d\,^{2}D$, $4s\,^{2}S$, $4p\,^{2}P^{o}$, $5p\,^{2}P^{o}$	22	$4p\,^{2}P^{o}$, $5p\,^{2}P^{o}$
Si I	$3p\,^{1}D$, $3d\,^{3}P^{o}$, $3d\,^{3}D^{o}$, $4s\,^{3}P^{o}$, $4d\,^{3}D^{o}$	13	$3d\,^{3}P^{o}$, $3d\,^{3}D^{o}$, $4s\,^{3}P^{o}$, $4d\,^{3}D^{o}$
Si II	$4d\,^{2}D$, $3s\,3p^{2}\,^{2}P$, $3d\,^{2}D$, $3p\,^{2}S$, $4s\,^{2}S$	…	$4d\,^{2}D$, $3s\,3p^{2}\,^{2}P$, $3d\,^{2}D$, $3p\,^{2}S$, $4s\,^{2}S$
S I	$4s\,^{3}S^{o}$, $4s'\,^{3}D^{o}$, $3d\,^{3}D^{o}$, $5s\,^{3}S^{o}$,	…	$4s\,^{3}S^{o}$, $4s'\,^{3}D^{o}$, $3d\,^{3}D^{o}$, $5s\,^{3}S^{o}$,
	$6s\,^{3}S^{o}$, $4s''\,^{3}P^{o}$	…	$6s\,^{3}S^{o}$, $4s''\,^{3}P^{o}$
S II	$3s\,3p^{4}\,^{4}P$	…	$3s\,3p^{4}\,^{4}P$
Ar I	$4s\,^{3}P^{o}$, $4s\,^{1}P^{o}$	…	$4s\,^{3}P^{o}$, $4s\,^{1}P^{o}$
Ca I	$4p\,^{1}P^{o}$, $4p'\,^{1}P^{o}$	…	$4p\,^{1}P^{o}$, $4p'\,^{1}P^{o}$
Ca II	$3d\,^{2}D$, $4p\,^{2}P^{o}$, $4d\,^{2}D$, $5s\,^{2}S$, $5p\,^{2}P^{o}$	23, 24	…

REFERENCES.—(1) Callaway (1982); (2) Callaway (1985); (3) Callaway et al. (1987); (4) Itikawa (1986); (5) de Heer, McDowell, & Wagenaar (1977); (6) Whelan (1986); (7) Berrington & Kingston (1987); (8) McDowell (1985); (9) Katiyar & Srivastava (1988); (10) Berrington et al. (1985); (11) Jobe & St. John (1967); (12) St. John, Miller, & Lin (1964); (13) Pindzola, Bhatia, & Temkin (1977); (14) Thomas & Nesbet (1975); (15) Henry, Burke, & Sinfailam (1969); (16) Ganas (1981); (17) Tayal & Henry (1989); (18) Laher & Gilmore (1990); (19) Msezane (1988a); (20) Ganas (1985); (21) Leep & Gallagher (1976); (22) Chidichimo (1988); (23) Msezane (1988b); (24) Mitroy et al. (1988).

In Table 6 all the included levels and the references for cross sections are listed. Where no reliable determinations, theoretical and experimental, exist, the Bethe approximation is used (Van Regemorter 1962). The Bethe approximation is only accurate to a factor of about 2 at low energies, but should for the resonance transitions give a reasonable estimate for the amount of energy going into excitation. At high energies this approximation is fairly accurate. The oscillator strengths for most transitions, except for iron, are taken from Wiese & Martin (1980) and Morton & Smith (1973).

Oscillator strengths for Fe I and Fe II are taken from Axelrod (1980). The Bethe approximation is used for all allowed transitions for iron. For Fe I we have averaged the oscillator strengths from the ground state multiplet, $a\ ^{5}D$, to the 16 lowest multiplets, connected to the ground state by allowed transitions. The fine-structure levels of $a\ ^{5}D$ are assumed to be in LTE at a temperature of 3000 K. The results are not sensitive to this temperature as long as it is above $\sim$1400 K.

For Fe II we have included averages from the ground state multiplet, $4s\ a\ ^{6}D$, to the sextet levels $4p\ z\ ^{6}D$ (4.75 eV), $4p\ z\ ^{6}F$ (5.18 eV), $4p\ z\ ^{6}P$ (5.29 eV). Transitions to the quartet multiplets $4p\ z\ ^{4}F$, $4p\ z\ ^{4}D$, $4p\ z\ ^{4}P$, and the doublet $4s\ c\ ^{2}F$ are included as one level at 5.56 eV. All allowed transitions between the first excited multiplet $3d\ a\ ^{4}F$ to the excited multiplets above are included as one transition. The population of the $3d\ a\ ^{4}F$ level relative to the ground state is assumed to be in LTE at 3000 K. The forbidden transitions between the ground state $4s\ a\ ^{6}D$ and the $a\ ^{6}S$, $a\ ^{4}P$, $b\ ^{4}P$, $a\ ^{4}D$, $b\ ^{4}D$, $b\ ^{4}F$, $a\ ^{4}G$, and $a\ ^{4}H$ levels are grouped in four energy groups and then averaged. Here no clear division between different excited multiplets is made. In the same way, five energy groups are used from $3d\ a\ ^{4}F$ to the forbidden levels. For the forbidden transitions we assume that the cross section behaves as $\sigma \propto \Omega/E$, where Ω is the low-energy collision strength, taken from Nussbaumer & Storey (1980).

REFERENCES

Aitken, D. K., Smith, C. H., James, S. D., Roche, P. F., Hyland, A. R., & McGregor, P. J. 1988, MNRAS, 235, 19P
Allen, C. W. 1973, Astrophysical Quantities, 3d ed. (London: Athlone)
Arnaud, M., & Rothenflug, R. 1985, A&AS, 60, 425
Axelrod, T. S. 1980, Ph.D. thesis, Univ. California, Santa Cruz
Bell, K. L., Dalgarno, A., & Kingston, A. E. 1968, J. Phys. B, 1, 18
Berrington, K. A., Burke, P. G., Freitas, L. C. G., & Kingston, A. E. 1985, J. Phys. B, 18, 4135
Berrington, K. A., & Kingston, A. E. 1987, J. Phys. B, 20, 6631
Callaway, J. 1982, Phys. Rev. A, 26, 199
———. 1985, Phys. Rev. A, 32, 775
Callaway, J., Unnikrishnan, K., & Oza, D. H. 1987, Phys. Rev. A, 36, 2576
Chidichimo, M. C. 1988, Phys. Rev. A, 37, 4097
Chugai, N. N. 1987, Soviet Astron. Lett., 13, 282
Colgate, S. A., & McKee, C. 1969, ApJ, 157, 623
Dalgarno, A., & Lejeune, G. 1971, Planet Space Sci., 19, 1653
Danziger, I. J., Bouchet, P., Gouiffes, C., & Lucy, L. B. 1991, in ESO/EIPC Workshop Supernova 1987A and Other Supernovae, ed. I. J. Danziger & K. Kjär (Garching: ESO), 217
de Heer, F. J., McDowell, M. R. C., & Wagenaar, R. W. 1977, J. Phys. B, 10, 1945
Douthat, D. A. 1975a, Radiation Res., 61, 1
———. 1975b, Radiation Res., 64, 141
Escalante, V., & Victor, G. A. 1990, ApJS, 73, 513
Fransson, C. 1991 in Supernovae (Les Houches, Session LIV 1990), ed. J. Audouze, S. Bludman, R. Mochkovitch, & J. Zinn-Justin (New York: Elsevier), in press
Fransson, C., & Chevalier, R. A. 1987, ApJ, 322, L15
———. 1989, ApJ, 343, 323
Fryxell, B., Müller, E., & Arnett, D. 1991, ApJ, 367, 619
Ganas, P. S. 1981, Physica, 104C, 411
———. 1985, J. Appl. Phys., 57, 154

Hachisu, I., Matsuda, T., Nomoto, K., & Shigeyama, T. 1990, ApJ, 358, L57
Hashimoto, M., Nomoto, K., & Shigeyama, T. 1989, A&A, 210, L5
Henry, R. J. W., Burke, P. G., & Sinfailam, A. -L. 1969, Phys. Rev., 178, 218
Herant, M., & Benz, W. 1991, ApJ, 370, L81
Hummer, D. G., & Rybicki, G. B. 1985, ApJ, 293, 258
Inokuti, M. 1990, in Molecular Processes in Space, ed. T. Watanabe, I. Shimamura, M. Shimizu, & Y. Itikawa (Plenum: New York), 65
Itikawa, Y. 1986, Phys. Rep., 143, 69
Jobe, J. D., & St. John, R. M. 1967, Phys. Rev., 164, 117
Johnson, L. C. 1972, ApJ, 174, 227
Katiyar, A. K., & Srivastava, R. 1988, Phys. Rev. A, 38, 2767
Kirshner, R. P., & Kwan, J. 1975, ApJ, 197, 415
Laher, R. R., & Gilmore, F. R. 1990, J. Phys. Chem. Ref. Data, 19, 277
Leep, D., & Gallagher, A. 1976, Phys. Rev. A, 13, 148
Lucy, L. B. 1991, ApJ, 383, 308
McDowell, M. R. C. 1985, Electron Impact Excitation of Atomic Helium (Atomic Data Workshop; Proc. Daresbury Study Weekend 29–31 March 1985), 19
Mitroy, J., Griffin, D. C., Norcross, D. W., & Pindzola, M. S. 1988, Phys. Rev. A, 38, 3339
Morton, D. C., & Smith, W. H. 1973, ApJS, 26, 333
Moseley, S. H., Dwek, E., Glaccum, W., Graham, J. R., Loewenstein, R. F., & Silverberg, R. F. 1989, ApJ, 347, 1119
Msezane, A. Z. 1988a, Phys. Rev. A, 37, 1787
———. 1988b, J. Phys. B, 21, L61
Nomoto, K., & Hashimoto, M. 1988, Phys. Rep., 163, 13
Nussbaumer, H., & Storey, P. J. 1980, A&A, 89, 308
———. 1983, A&A, 126, 75
———. 1986, A&AS, 64, 545
Opal, C. B., Peterson, W. K., & Beaty, E. C. 1971, J. Chem. Phys., 55, 4100
Osterbrock, D. E. 1989, Astrophysics of Gaseous Nebulae and Active Galactic Nuclei (Mill Valley: University Science)
Peterson, L. R., & Green, A. E. S. 1968, J. Phys. B, 1, 1131
Phillips, M. M., & Williams, R. E. 1991, in Supernovae, Proc. 10th Santa Cruz Summer Workshop in Astronomy and Astrophysics, ed. S. E. Woosley (Berlin: Springer), 36
Pindzola, M. S., Bhatia, A. K., & Temkin, A. 1977, Phys. Rev. A, 15, 35
Saio, H., Nomoto, K., & Kato, M. 1988, Nature, 334, 508
Schunk, R. W., & Hays, P. B. 1971, Planet. Space Sc., 19, 113
Shigeyama, T., & Nomoto, K. 1990, ApJ, 360, 242
Shigeyama, T., Nomoto, K., & Hashimoto, M. 1988, A&A, 196, 141
Shull, J. M. 1979, ApJ, 234, 761
Shull, J. M., & Van Steenberg, M. E. 1985, ApJ, 298, 268
Spencer, L. V., & Fano, U. 1954, Phys. Rev., 93, 1172
Spitzer, L., & Tomasko, M. G. 1968, ApJ, 152, 971
St. John, R. M., Miller, F. L., & Lin, C. C. 1964, Phys. Rev., 134, A888
Stolarski, R. S., & Green, A. E. S. 1967, J. Geophys. Res., 72, 3967
Swartz, D. A. 1989, Ph.D. thesis, Univ. Texas
———. 1991, ApJ, 373, 604
Tayal, S. S., & Henry, R. J. W. 1989, Phys. Rev. A, 39, 4531
Thomas, L. D., & Nesbet, R. K. 1975, Phys. Rev. A, 12, 2378
Van Regemorter, H. 1962, ApJ, 136, 906
Voit, M. 1991, ApJ, 377, 158
Whelan, C. T. 1986, J. Phys. B, 19, 2355
Wiese, W. L., & Martin, G. A. 1980, Wavelengths and Transition Probabilities for Atoms and Atomic Ions, Part 2 (Washington: NBS)
Woosley, S. E. 1988, ApJ, 330, 218
Woosley, S. E., Arnett, W. D., & Clayton, D. D. 1973, ApJS, 26, 231
Woosley, S. E., & Weaver, T. A. 1986, in Radiation Hydrodynamics in Stars and Compact Objects, ed. D. Mihalas & K. H. Winkler (Berlin: Springer), 91
Xu, Y. 1989, Ph.D. thesis, Univ. Colorado, Boulder
Xu, Y., & McCray, R. 1991a, in Supernovae, Proc. 10th Santa Cruz Summer Workshop in Astronomy and Astrophysics, ed. S. E. Woosley (Berlin: Springer), 444
———. 1991b, ApJ, 375, 190
Xu, Y., McCray, R., Oliva, E., & Randich, S. 1992, ApJ, 386, 181